NUMERICAL MODELING OF THE METAL MELTING UTILIZING A DC ELECTRIC ARC PLASMA FOR ELECTRIC ARC FURNACE

by

Yu Wang

A Thesis

Submitted to the Faculty of Purdue University

In Partial Fulfillment of the Requirements for the degree of

Master of Science in Mechanical Engineering
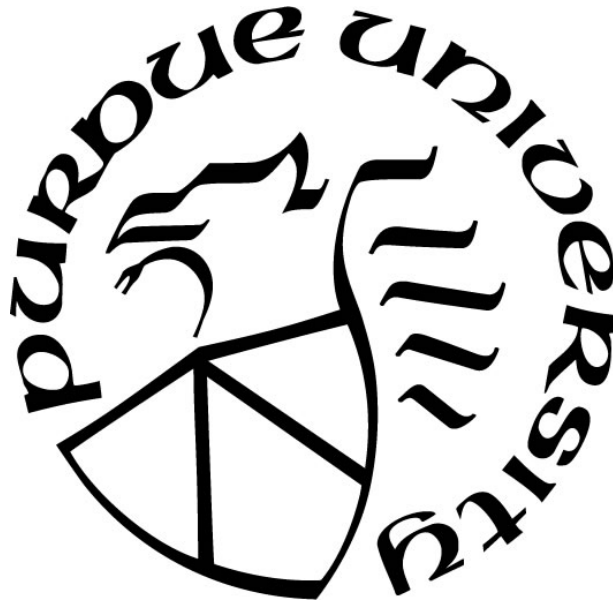
Department of Mechanical and Civil Engineering

Hammond, Indiana

December 2019

THE PURDUE UNIVERSITY GRADUATE SCHOOL
STATEMENT OF COMMITTEE APPROVAL

Dr. Chenn Q. Zhou, Chair

Department of Mechanical and Civil Engineering

Dr. Xiuling Wang

Department of Mechanical and Civil Engineering

Dr. Ran Zhou

Department of Mechanical and Civil Engineering

Approved by:

Dr. Chenn Q. Zhou

To my parents

ACKNOWLEDGMENTS

TABLE OF CONTENTS

LIST OF TABLES

LIST OF FIGURES

NOMENCLATURE

e	Electron charge	J_{max}	Maximum current density
K_B	Boltzmann's constant	r_h	Radius of the "white hot"
$\vec{v}$	Velocity vector	I	Current
$T_{e,a}$	Temperature of the plasma column adjacent to the electrode	D	Binary diffusion coefficient between arc plasma and anode material
σ	Electrical conductivity	χ_i	Mass fraction of at the anode surface
J_a	Current density	β	Thermal expansion coefficient
V_w	Anode work function	u	Axial velocity
V_a	Anode fall voltage	v	Radial velocity
C_1	0.515	μ	Viscosity
C_2	0.11	j_r	Radial current density component
Pr	Prandtl number	j_x	Axial current density component
ρ	Density	B_θ	Azimuthal magnetic induction
μ	Viscosity	c_p	Specific heat
v_r	The radial velocity	T	Temperature
h	Enthalpy	k	Thermal conductivity
a	Values at the anode surface	μ_0	Magnetic permeability
b	Values at the edge of boundary layer in plasma	P_v	Saturating vapor pressure of the material
$S_{r,j}, S_r$	Radiation heat loss	V	Electrical potential
ΔV_j	Volume element	T_r	Reference temperature
$r_{i,j}$	Vector joining the surface i and volume j	ϕ	Coefficient of thermal diffusion of electrons

W_e	Mass evaporation rate	M_{mat}	The molar friction of the material
L_v	Latent heat of vaporization	M_{pla}	The molar friction of the plasma
Q_E	Heat transfer of electronic flow	k	Kinetic energy
Q_v	Heat transfer of metal vaporization	ε	Turbulence dissipation rate
Q_c	Heat transfer of convection	Q_r	Heat transfer of radiation
G_k	Generation of turbulence kinetic energy	G_b	Generation of turbulence kinetic energy
ψ_i	Angle between $r_{i,j}$ and the normal vector of the surface	ξ	A small number to prevent division by zero
$C_{1\varepsilon}$	1.44	β	Liquid fraction
$C_{2\varepsilon}$	1.92	ΔH	Latent heat
c_μ	0.09	A_{mush}	Mushy zone constant
σ_k	1.0	δ	Thickness of the anode interface
σ_ε	1.3	$\overrightarrow{v_p}$	Solid velocity
$\emptyset$	The turbulence quantity	F	Volume of fluid fraction
J	Current density	φ_a	Work function of the anode
k_{eff}	Effective thermal conductivity	T_a	Metal anode temperature
Y_M	Contribution of the fluctuating dilatation in compressible turbulence to the overall dissipation rate		

ABSTRACT

The electric arc furnace (EAF) is one of the most widely-used steelmaking process recycling the scrap as the raw material. Electric arc furnace steelmaking is a material-dependent and energy-consuming process. The electricity is utilized as the main heat source to melt the scrap by the electric arc discharging from the graphite electrodes. Since the plasma arc weld has the very similar heat transfer mechanism and melting phenomenon comparing with the scrap melting in EAF process, the model development for the free-burning arc, the arc-metal heat transfer, and the metal melting will refer to the research of plasma arc weld field and start with a relatively small scale. In this study, a comprehensive computational dynamics (CFD) model was developed to predict the heat transfer from the electric arc to the metal anode, which is composed of the DC electric arc model, solidification and melting model, and the arc-metal heat transfer model. The validation of the CFD models has been conducted utilizing the experimental data and simulation results in other literature. The commercial software, ANSYS FLUENT®, was employed with the User-Defined Function scripts and the User-Defined Scalar to model the magnetic field, comprehensive flow field, and high temperature field. Furthermore, the parametric studies for the process of the anode melted by the plasma arc were performed to investigate the effects of the arc current and the initial anode temperature on the anode melting. The results reveal that the value of the arc current has a positive correlation with the arc temperature and velocity but has negative correlation with the penetration time of the anode. Meanwhile, with the increase of anode initial temperature, the metal penetrate time will decrease.

CHAPTER 1. INTRODUCTION

1.1 Electric Arc Furnace Steelmaking – Development and Industrial Process

The steel industry plays a critical role to the United States. As the raw material of traditional manufacturing, transportation, construction and kinds of consumer merchandise, steel is also widely used in the modern petrochemical industry, marine development, etc. In 2011, the U.S. steel industry produced commercial products of which the value was estimated as $103 billion, which represented worldwide 6% of crude steel production. Due to the strength, steel became the most popular recycled material and a huge amount of it is produced by the scrap in the United States. However, the electric arc furnace (EAF) is one of the most representative steelmaking processes recycling the scrap as the raw material. The scrap as one of the raw materials plays a crucial role for the charged material because of the flexibility in material utilization and is also less capital intensive. During the past 60 years, steel scrap consumed by EAFs has increased rapidly. In 2013, EAFs have contributed approximately 30 percent to the steel production worldwide [1]. The productivity of crude steel from EAFs is expected to keep increasing to reach 872 million tons in 2050 [2].
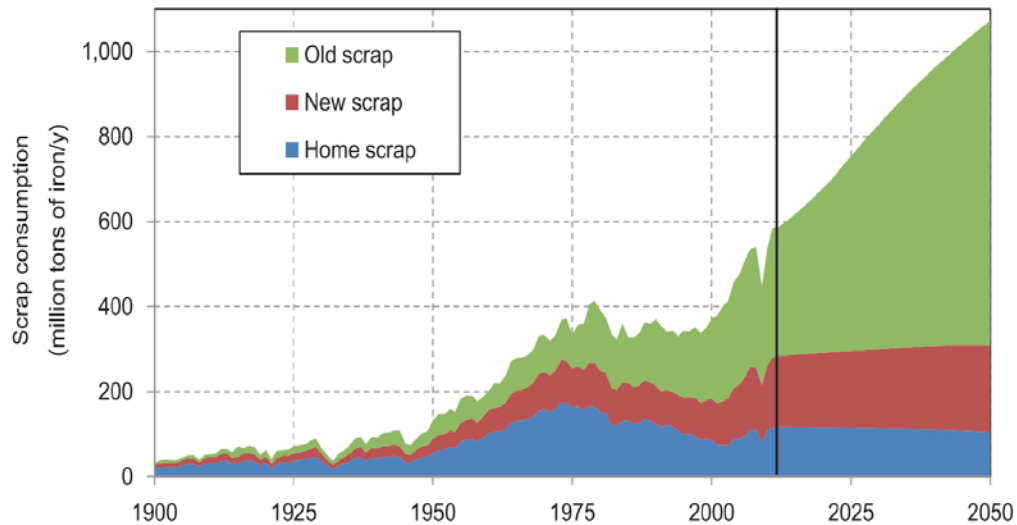
Figure 1. Scrap consumption trends in steel and foundry sectors [20].
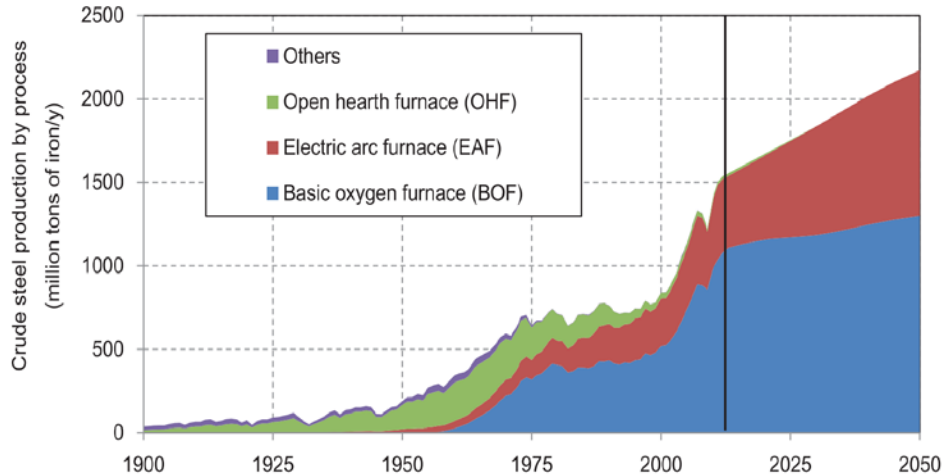
Figure 2. Crude steel production by processes [20].

Héroult in France developed the alternative energy source of coal from the arc high temperature of the electrode from 1888 to 1892, and invented the electric arc furnace of industrial direct smelting. At first, the electric arc furnace was only used for the production of calcium carbide and ferroalloys. It was not until 1906 that EAFs were developed for steelmaking, which enabled the recycling of scrap steel to be economical and large-scale. The electric arc furnace converts electrical energy into heat by an arc occurring between the end of the graphite electrode and the charged materials. Then the charged materials will be melted and the subsequent thermometallurgical reaction is completed. With the development of the power industry, the continuous improvement of process equipment and smelting technology, the application of electric arc furnaces is becoming more and more extensive.

The production capacity and scale are increasing as well. In the 1930s, the maximum capacity of the electric arc furnace was 100t. In the early 1970s, a 400t electric arc furnace was put into production. Especially in the past 50 years, the technical performance of electric arc steelmaking furnace has gradually improved and the production cost has dropped significantly. The proportion of electric arc furnace steelmaking in developed countries in Europe and America has exceeded 50%. Generally, there are two types of EAF, which are DC EAF and AC EAF. They both use electric arc to melt the scrap. DC EAF has some advantages over an AC EAF. The first is the arc is more stable and concentrated, which leads less erosion of the furnace wall. The temperature distribution in the furnace is more even. The second is the fluctuations of current and voltage is

weaker, which prolongs the cable life. The third is the reduction of the electrodes' consumption. However, DC EAF has been suffering from the inability to obtain high-power DC power source, which greatly limits its development.
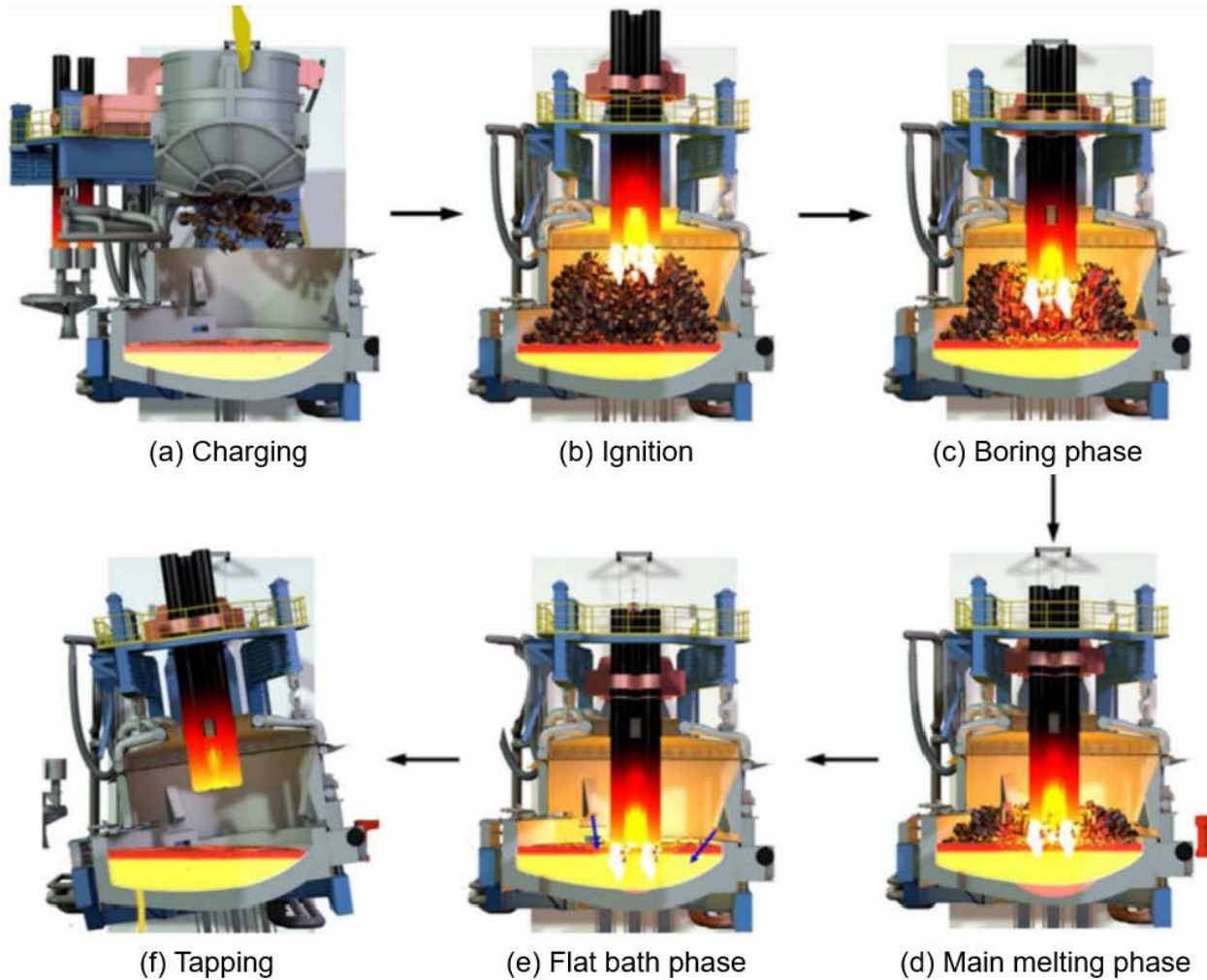
Figure 3. A typical AC EAF process [19].

The EAF steelmaking process can be crudely divided into four stages: furnace charging, melting, refining, and tapping. This operation cycle is also known as the tap to tap cycle. The melting stage and refining stage are the primary productive process. After the scrap charging, the electrodes are lowered and an intermediate voltage tap is applied until the electrodes has bored into the scrap. Approximately 15% of the scrap can be melted during the initial bore-in period [3]. Later, when the electrodes penetrate the scrap, voltage tap is able to be applied without worrying about the

damage of the arc to the roof and furnace walls. During this process, the electrode breaks down the air and generate the electric arc between the electrodes' tip and the scrap. The energy is transferred from the electrode tip to the scrap so that it can be heated. Generally, approximately 50% to 60% of the energy which is used to melt the scrap is supplied by the electrical energy. In addition, the behavior of the arc and its stability has a great influence to the productive efficiency and quality, even more on the safety of the entire production process. About 18 to 20 minutes later, most scrap is melted and the refining stage starts. During refining stage, the decarburization and other impurities removal by injected oxygen will be more focused on.

1.2   Electric Arc and its Heat Transfer Mechanism

Electric arc is a gas discharge phenomenon as well as an instantaneous spark generated by an electric current through some insulating media such as argon and air, which is also a plasma. The plasma is the fourth state of the substance juxtaposed with solids, liquids, and gases. Usually, the plasma arc is divided into an arc column region, a cathode region, and an anode region. The cathode region connects the cathode and the arc column, which contains an ionization region and a cathode sheath. The charged particle is generated in the ionization region and the cathode sheath is a significant place which maintains the electric conductivity in the cathode region. Vast electrons are emitted from the cathode spot. While the arc is discharging, not all the cathode participates in the discharge process. The discharge happens on the cathode surface and is only concentrated on a small area called the cathode spot. The cathode spot with a very large current density is the source of powerful electron flow in arc discharge, which is very bright and concentrated. In the arc column, the medium particles collide with each other to produce free electrons and positive ions. Simultaneously, some electrons and positive ions recombine into neutral particles or diffuse outside the arc column.

Arc thermal plasma generally follows the thermodynamic state: the complete thermodynamic equilibrium state, the local thermodynamic equilibrium (LTE) state, and the double-temperature plasma. The complete thermodynamic equilibrium state is an ideal thermodynamic state that is difficult to achieve in practical experiments and industry. Double-temperature plasma means that because the electron temperature is low or the concentration gradient is large, the electrons cannot diffuse sufficiently and the energy of the electrons cannot be transmitted by the collision, which

16

means the electron temperature is significantly higher than the heavy particle temperature. The arc column generally satisfies the local thermodynamic equilibrium state, which means the temperature of each particle in the arc is uniform. In the anode region, the anode spot like the cathode spot is also existing on the anode surface. Not only are the electrons collected by the anode through the anode spot, but also the metal vapor is produced by the anode surface which can supply the charged particle to the arc column [4].
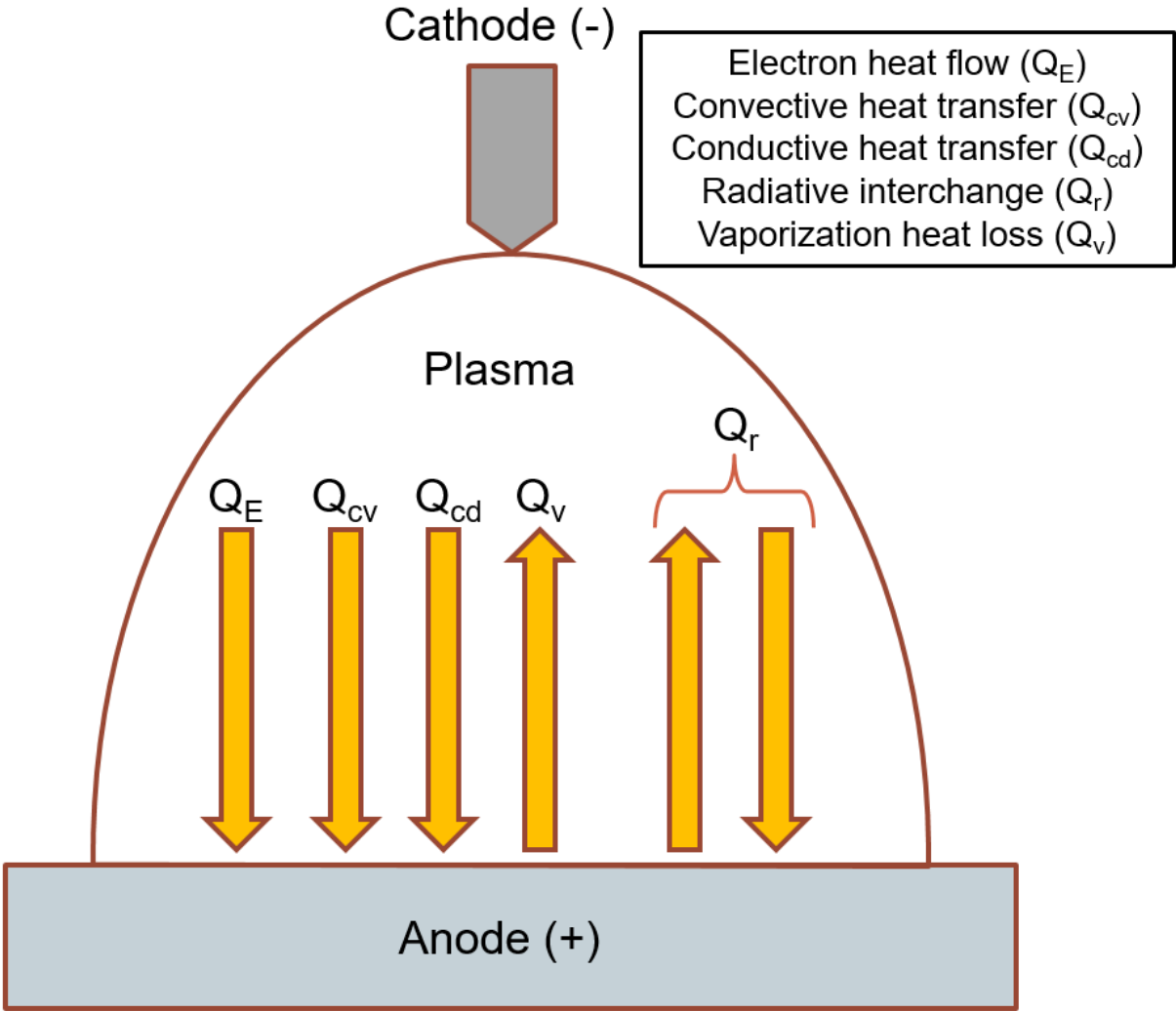
Figure 4. Schematic diagram of the heat transfer mechanism between the arc and anode.

The heat transfer between the electric arc and the metal anode mainly happens on the anode spot, which is contributed by the convective heat transfer, conductive heat transfer, and radiative interchange heat transfer because of the electron flow and the heat loss due to metal vaporization.

Mckelliget and Szekely [5] investigated the mechanisms of heat and momentum transferring from plasma arc to anode boundary layer. In the classical theory of the heat transfer from the plasma arc to the anode, a positive voltage drop (the anode fall voltage) exists. The electron heat flow to the anode is consisted of random thermal energy transport of electrons, Thomson effect, and condensation heat transfer (anode fall and work function), which can be expressed as:

$$Q_E = \frac{\left(\frac{5}{2} + \frac{e\phi}{K_B\sigma}\right)J_a K_B T_{e,a}}{e} + J_a V_w + J_a V_a \qquad [1]$$

where e is electron charge, ϕ is coefficient of thermal diffusion of electrons, K_B is Boltzmann's constant, $T_{e,a}$ is the temperature of the plasma column adjacent to the electrode, σ is electrical conductivity of plasma, J_a is current density, V_w is anode work function, V_a is the anode fall voltage.

The convective heat transfer term is combined with a real convective heat transfer due to the motion of the plasma impacting the anode and a pure conduction, which can be expressed as:

$$Q_c = \frac{C_1}{Pr_a}\left(\frac{\rho_b \mu_b}{\rho_a \mu_a}\right)^{C_2}\left(\rho_a \mu_a \frac{dv_r}{dr}\right)^{0.5}(h_b - h_a) \qquad [2]$$

where C_1 and C_2 are constant coefficients which are 0.515 and 0.11, respectively. Pr_a is Prandtl number, ρ is density, μ is viscosity, v_r is the radial velocity, h is enthalpy, the subscript a denotes values at the anode surface and b denotes values at the edge of boundary layer in plasma.

The radiation heat transfer from plasma arc to the anode is calculated by approximate view factors. The radiative heat flux emitted from the volume element j to the surface element i can be described as:

$$Q_r = \sum \frac{S_{r,j} \cdot \cos\psi_i}{4\pi r_{i,j}^2} \cdot \Delta V_j \qquad [3]$$

where $S_{r,j}$ is the radiation loss from volume element ΔV_j in the arc column to the anode surface i, $r_{i,j}$ is the vector joining the surface i and volume j, ψ_i is the angle between $r_{i,j}$ and the normal vector of the surface.

The final contribution of the heat transfer at the anode surface needed to be considered is the metal vaporization heat loss, which is described as [43]:

$$Q_v = W_e L_v \qquad\qquad [\,4\,]$$

where W_e is the mass evaporation rate and L_v is the latent heat of vaporization.

In conclusion, the heat transfer happening at the anode surface can be written in a simplified form:

$$Q_{Total} = Q_E + Q_c + Q_r - Q_v \qquad\qquad [\,5\,]$$

1.3 Objective

This thesis intends to develop a reliable computational fluid dynamics (CFD) model of electric arc and its heat transfer for a full-scale industrial EAF, which can be used to predict the electric arc behavior and the phenomenon of scrap melting by the electric arc in the future. The primary content in this research is as follows:

1. To develop a comprehensive free-burning arc CFD model including the geometry and related mesh establishment for the free-burning arc and its interaction with the anode.
2. To couple the free-burning arc model with the arc-metal heat transfer model and the melting model in order to capture the phenomenon of the anode melted by the plasma arc.
3. To conduct a model validation through comparing the simulation results with the experiment data in order to prove the accuracy of developed model.
4. To conduct parametric studies and perform evaluations of the impact factors for the developed model, such as the quantity of the current, initial anode temperature.

CHAPTER 2. LITERATURE REVIEW

2.1 Electric Arc

2.1.1 Free-burning Argon Arc Plasma

The high-intensity free-burning argon arc has been learned and widely applied on electric arc melting, plasma cutting, plasma arc welding (PAW) and so on. In order to have a better understanding and improve industrial application of arc, the comprehensive mathematic and numerical model of electric arc is required. However, the extremely high temperature of the electric arc plasma which could reach up to 23000K and the interaction among electromagnetic field, thermal effect and fluid dynamic hampered development of the comprehensive modeling of the arc. Fortunately, after many researchers' efforts, the arc plasma model has made a major breakthrough in the past three decades. Hsu et al. [8] studied the free-burning high-intensity argon arc and developed an experimental work to investigate the arc behavior. A 2D steady-state model was also developed by solving the mass, momentum, energy, and current conservation equations. The "bell" shape of the arc as well as the temperature profile were obtained and shown in Figure 6, which corresponds to the experimental photograph shown in Figure 7. Through this 2D model, the effect of different current on the arc behavior was investigated as well. The most critical boundary condition for this model is the current density distribution along the boundary AD shown in Figure 5. Due to the limitation of the measurement, a reasonable profile was postulated and the form was assumed as:

$$j(r) = J_{max} \exp(-br) \qquad [\,6\,]$$

$$J_{max} = \frac{I}{2\pi r_h^2} \qquad [\,7\,]$$

where J_{max} and b are constant, I is the arc current, r_h is the radius of the "white hot" which approximately equal to 0.51 mm with 200 A current.
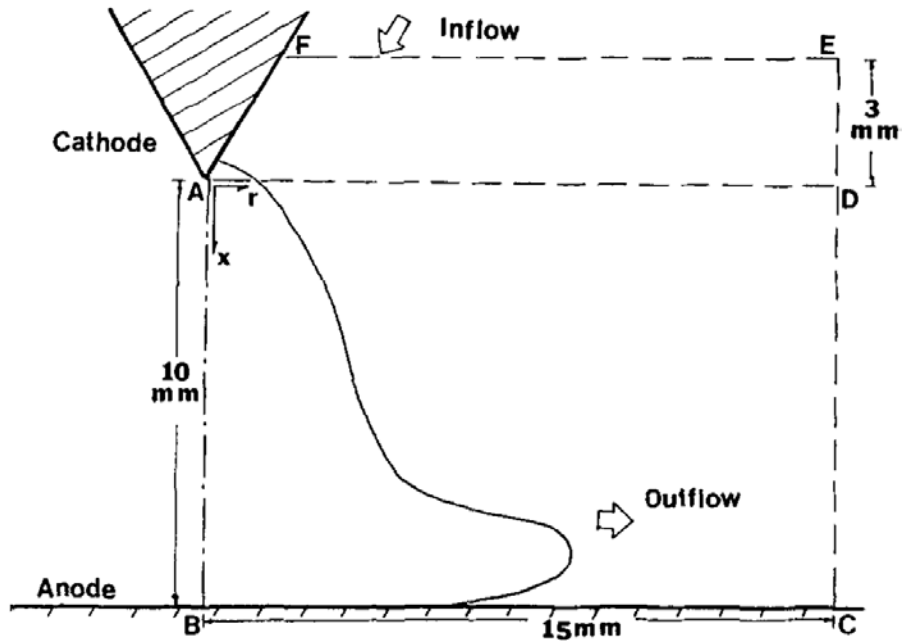
Figure 5. 2D Computation Domain [8].

ARGON   P = 1 ATM   I = 200A
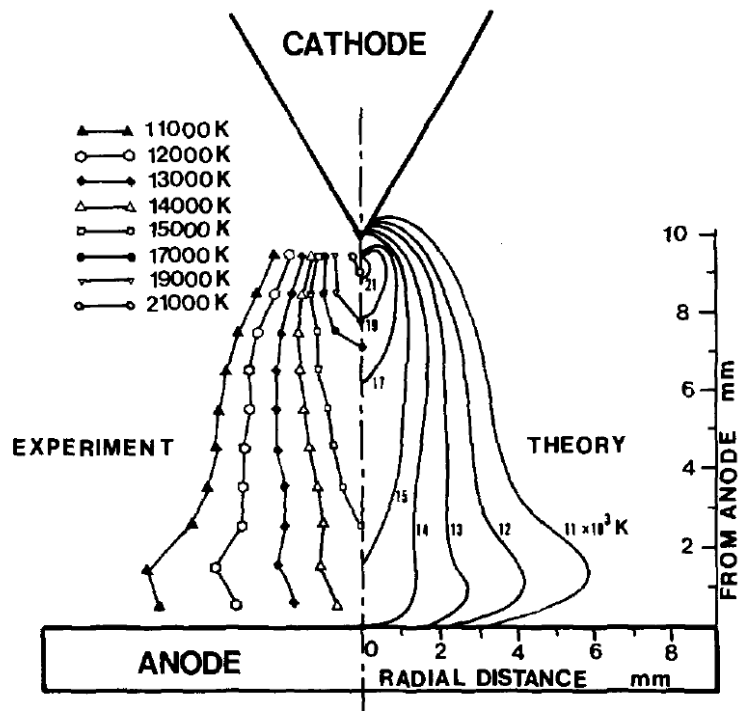
Figure 6. Comparison of temperature distribution between the simulation results and experimental measurement [8].
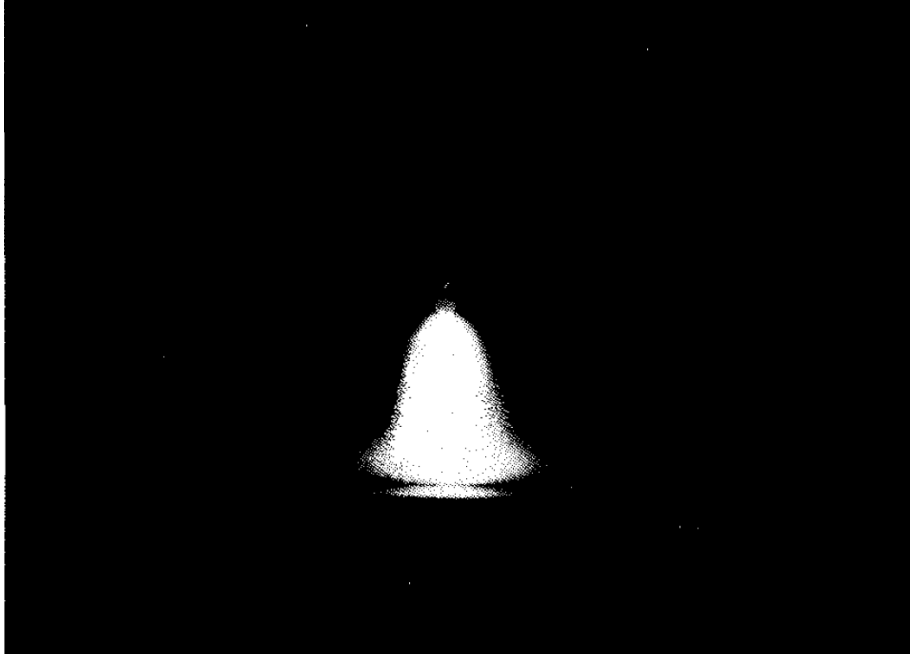
Figure 7. Photograph of the DC arc plasma in experiment [8].

2.1.2 Local Thermodynamic Equilibrium (LTE)

For the ionization of a gas atom, an ion or a molecule, if the number of heavy ions leaving a certain energy level per unit time is equal to the number of such particles reaching this energy level and the number of particles arriving at this level by a certain process is equal to the number of particles leaving the level at the opposite end of the process, this system is a global thermal equilibrium (GTE) system. However, in the spectral analysis, due to the presence of radiation exchange between light source (or atomizer, ionizer) and outside, the GTE is extremely difficult to achieve. Therefore, for any point, if the substance has the same temperature or the temperature is varying very slowly which can be negligible, one can assume the substance is in local thermodynamic equilibrium. LTE is a very popular assumption used for the electric arc prediction, which can simplify the computational process and greatly reduce computational time. Sansonnens [9] investigated the effects of non-LTE on a two-dimensional electric arc calculation. Lowke et al. [10] proposed a 'LTE-diffusion approximation' for the properties prediction of electric arc and compared with full diffusion calculation as well as the experimental data. With this approximation, the issues, which the equilibrium electrical conductivity of the arc around the electron is extremely

small, can be overcome. Figure 8 shows that the 'LTE-diffusion approximation' has very close agreement with the more accurate full diffusion method and the experimental data.
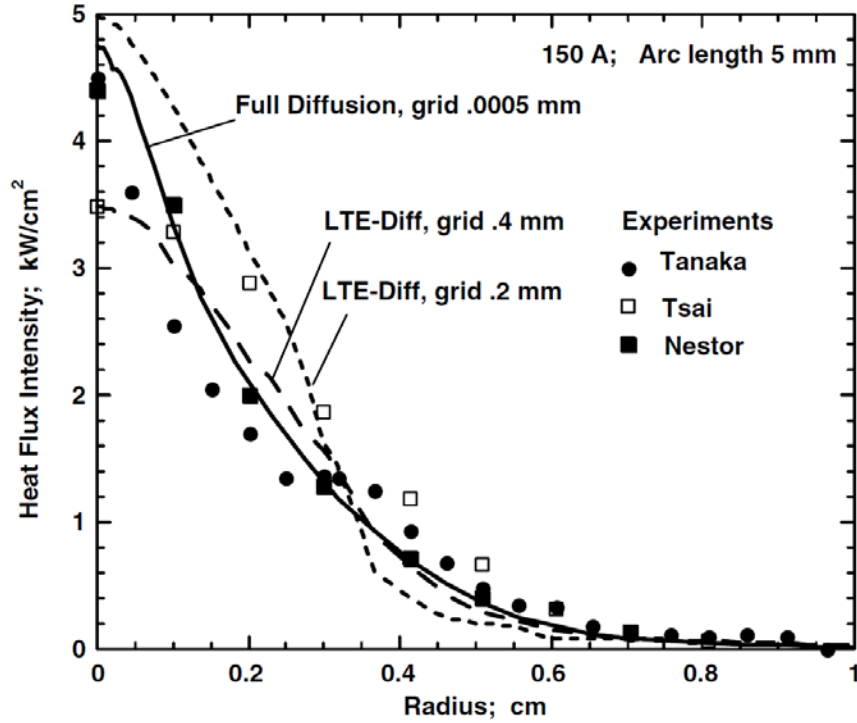
Figure 8. Comparison of the calculated heat flux densities at a copper anode for a 150A arc [10].

2.2 Heat Transfer between Electric Arc and Anode

2.2.1 Coupled Plasma-anode Model

Lago et al. and Gonzalez [11,12] developed a two dimensional model and a three dimensional model to simulate the arc behavior and its interaction with the anode. Besides, the effect of the metal vaporization of anode surface and the external forces on the arc column has been investigated. In order to sustain the current and energy conservation between the anode and the arc plasma, the corresponding relations was applied and expressed as follows:

$$\left(-k\frac{\partial T}{\partial x}\right)_{mat} = \left(-k\frac{\partial T}{\partial y}\right)_{pla} + j_z\left[\frac{5K_B}{2e}\left(T_{mat} - T_{pla}\right) + V_a + V_w\right] - L_{mat}\phi_V \qquad [8]$$

$$\left(-\sigma\frac{\partial V}{\partial x}\right)_{mat} = \left(-\sigma\frac{\partial V}{\partial y}\right)_{pla} \qquad [9]$$

23

$$\phi_v = \frac{1}{1-(\chi_i)_0}(\rho D)_0 \left(\frac{\partial \chi_i}{\partial z}\right)_0 \qquad [10]$$

$$\chi_i = \frac{P_v M_{mat}}{P_v M_{mat} + (1-P_v)M_{pla}} \qquad [11]$$

where K_B is Boltzmann's constant, e is electron charge, V_a is anode fall, V_w is the anode work function, L is the latent heat of the meatal vaporization, ϕ_V is the metal vaporization rate from the anode, χ_i is the mass fraction of at the anode surface, D is the binary diffusion coefficient between arc plasma and anode material, P_v is the saturating vapor pressure of the material, the subscript zero represents the values at the anode surface as indicated in [11]. M_{mat} and M_{pla} are the molar frictions of the material and arc plasma, respectively. Figure 9 shows the comparison of the temperature profile for the 2D and 3D model. The bell shape is obtained and the highest temperature reached 21000K, which is corresponding to most researchers' work [13-15].
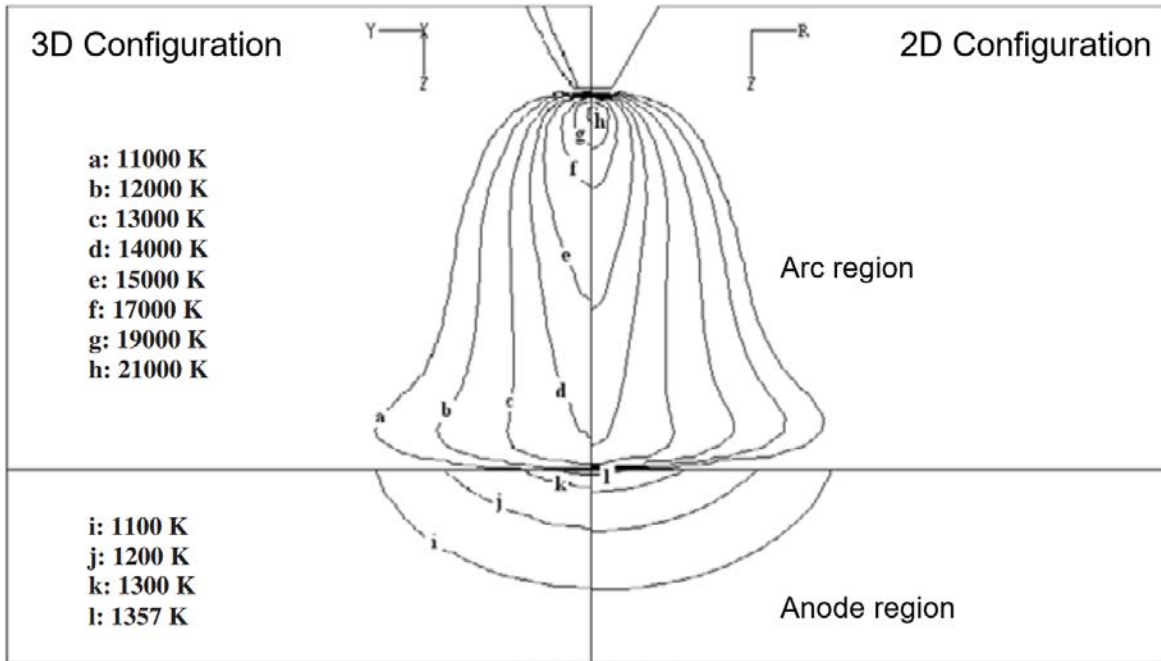
Figure 9. Comparison of the temperature profile of the arc and anode for 2D and 3D model [12].

Li el at. [16] developed a novel unified heat transfer model to predict the heat transfer between the arc and anode as well as the evolution of the keyhole formation in the welding pool, which is shown in Figure 10. The effect of the arc pressure and the heat flux at the anode surface were

considered and displayed with Gaussian distribution. This model greatly reduced the computational time and demonstrated good applicability and simplicity on the keyhole prediction.
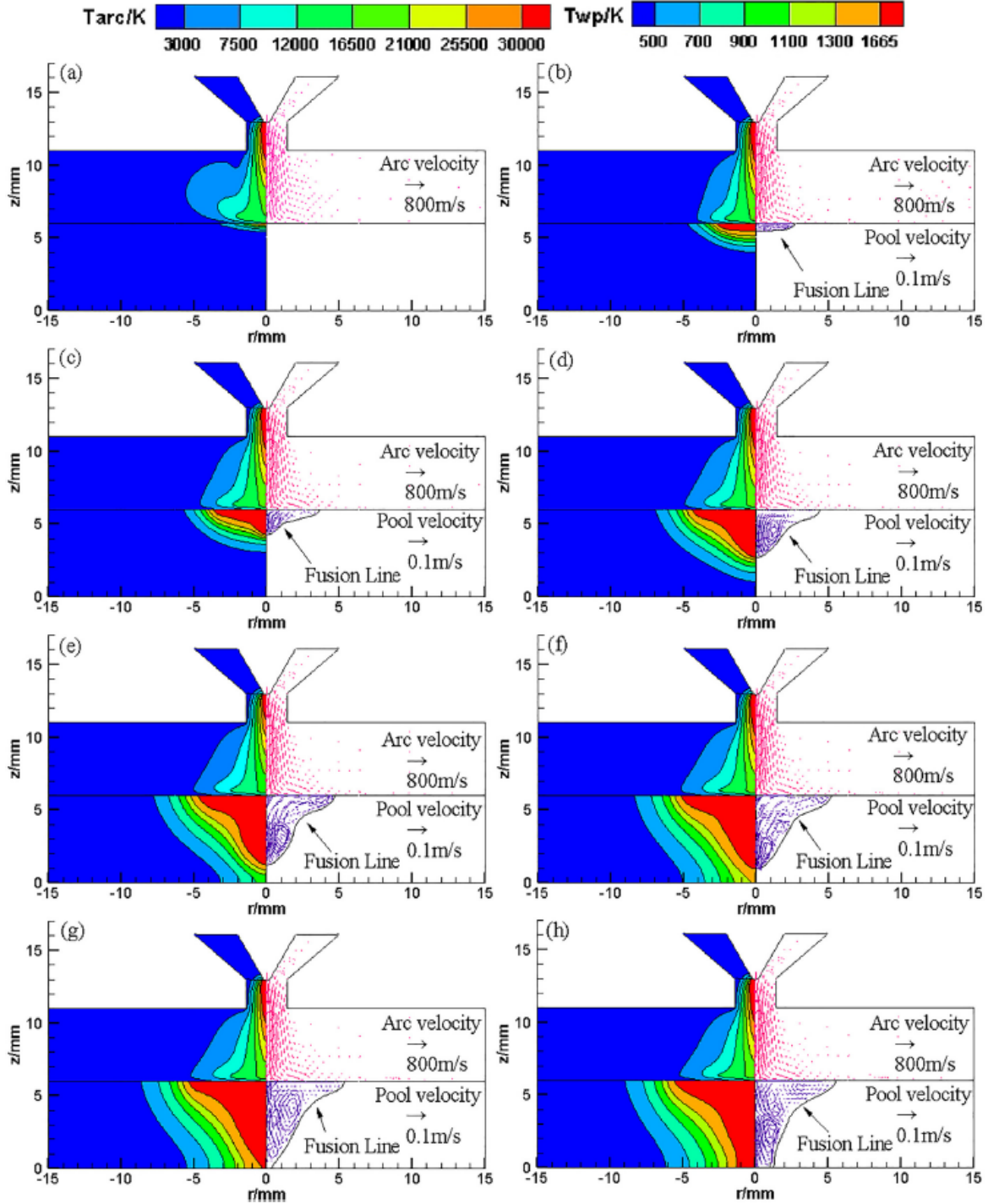
Figure 10. Dynamic evolutions of plasma arc and weld pool in the whole welding process. (a) t = 0.05 s (b) t = 0.2 s (c) t = 0.4 s (d) t = 0.8 s (e) t = 1.2 s (f) t = 1.6 s (g) t = 1.7 s (h) t = 1.8 s [16].

Jian and Wu [17] developed a unified fluid flow and heat transfer model to demonstrate the evolution of the arc plasma and the keyhole formation during the plasma arc welding process, which is shown in Figure 11. The transport mechanisms of the arc plasma, weld pool, and the keyhole in the stationary plasma arc welding were considered and coupled. In addition, the volume of fluid method and the "LTE-diffusion approximation" method were applied to track and treat the arc-metal interface where the additional source term was added to take the heat transfer into account. The enthalpy-porosity technique was also used to capture the melting phenomenon of the anode melting.
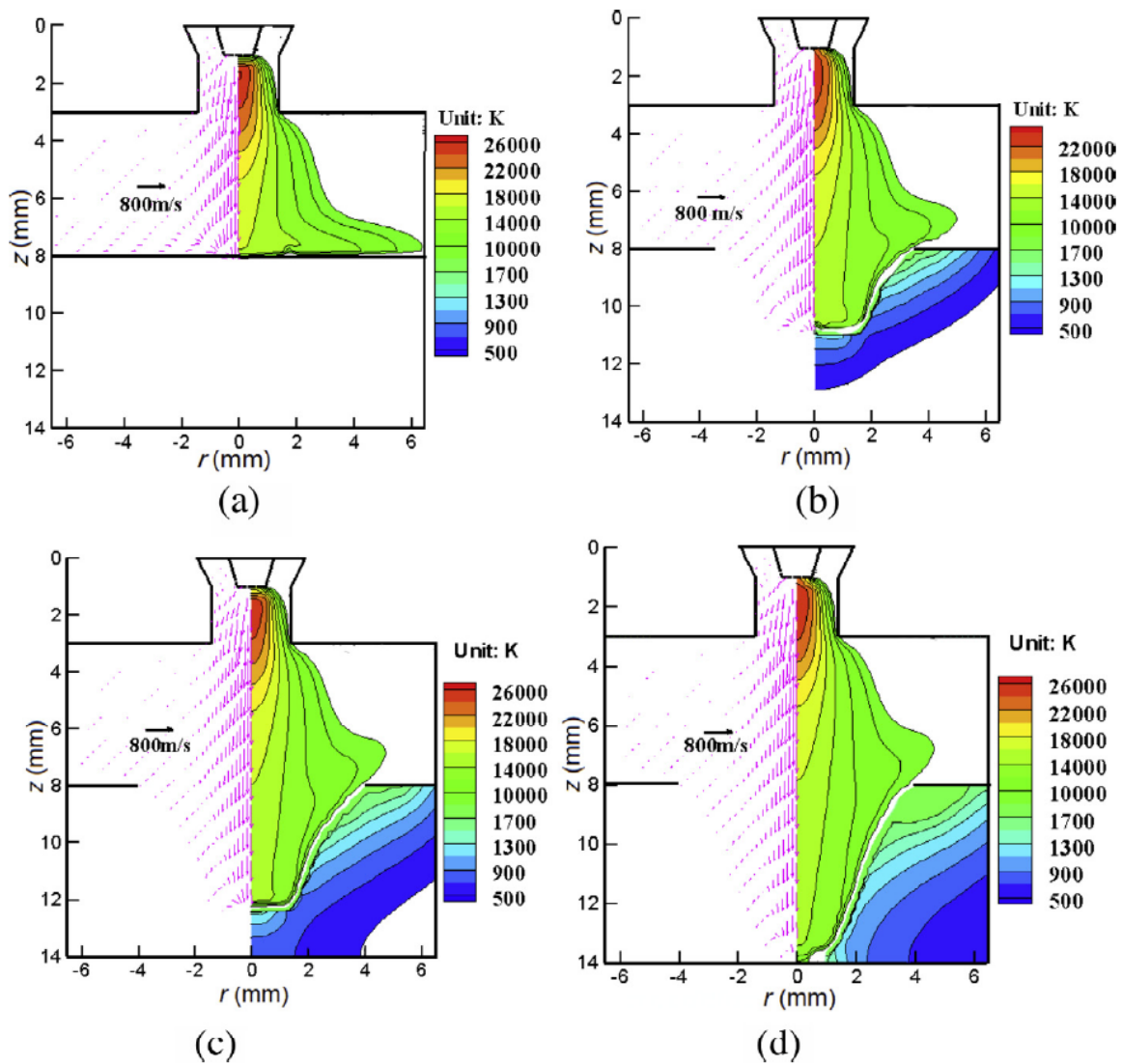
Figure 11. Evolution process of keyhole formation by arc plasma. (a) t = 0.001 s, (b) t = 0.5 s, (c) t = 1.0 s and (d) t = 1.48 s [17].

2.2.2 Fully Coupled Cathode-plasma-anode Model

Tanaka el at. [18] studied the free-burning argon arc with anode melting and developed a fully coupled unified numerical model to predict the distribution of temperature and velocity in the tungsten cathode, arc plasma and the anode work piece versus time for an arc welding process. Figure 12 shows the temperature distribution for the free-arc burning process versus time. Furthermore, the effect of the drag force of the cathode jet and the Marangoni force on the molten anode was investigated and compared.
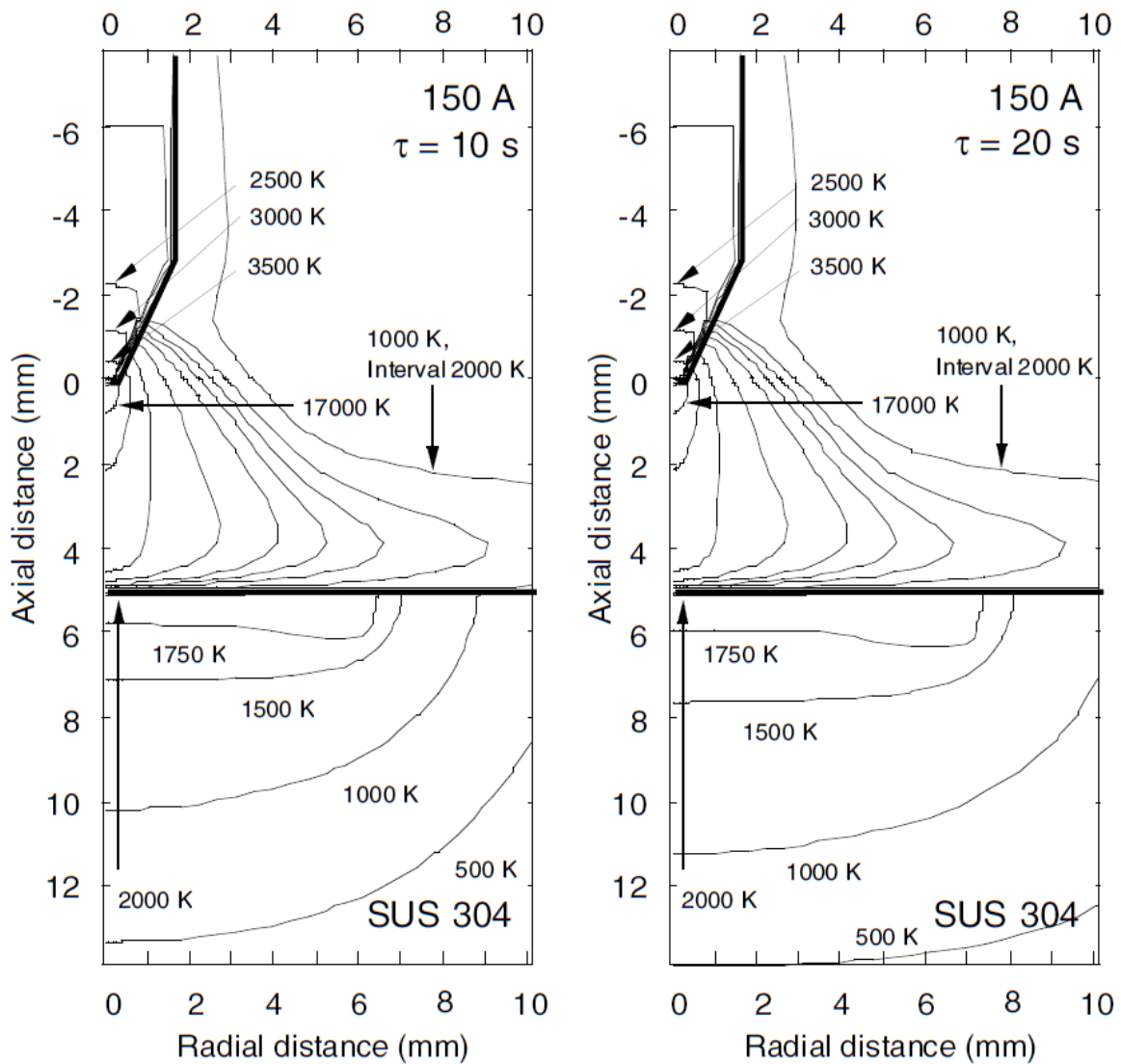
Figure 12. Predicted time dependent temperature contours for a 150 A in stationary welding process of SUS304 containing high sulfur [18].

Pan el at. [7] developed a two-dimensional coupled tungsten-plasma-anode mathematical model to predict and analyze the heat transfer and the fluid flow in a stationary keyhole plasma arc welding process. Besides, an experimental work was also conducted and the numerical calculated plasma arc pressure and the keyhole profile were validated with the experimental data. The volume of fluid method and the enthalpy-porosity technique were used to track the interface of anode and arc and deal with the mushy zone for metal anode melting process, respectively. Additional energy source term was added in the cathode-arc interface and the anode-arc interface in order to take the electronic heat transfer into account. Furthermore, the driving force was considered and quantitatively analyzed to understand the flow phenomenon in the molten pool. Figure 13 shows the evolution of the temperature profile of arc and anode as well as the keyhole formation after the arc ignition.
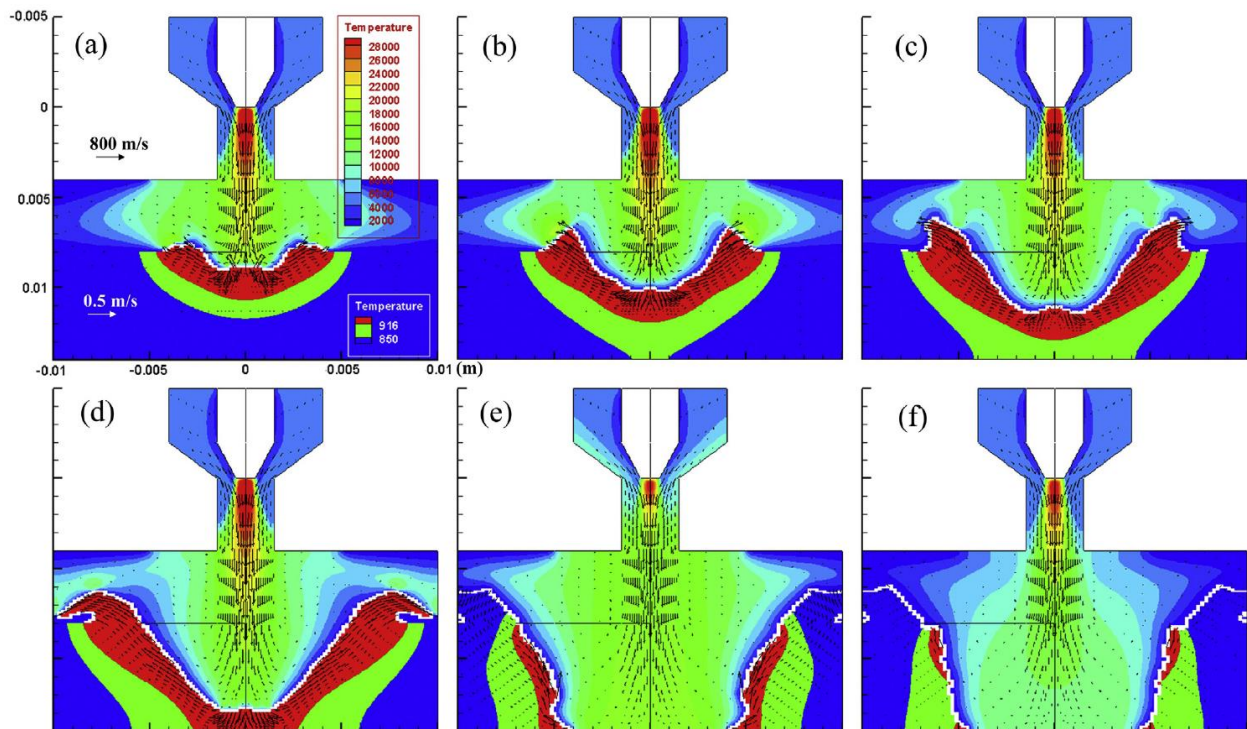
Figure 13. The keyhole evolution of temperature distribution and molten pool flow at (a) t = 0.52 s, (b) t = 0.72 s, (c) t = 0.92 s, (d) t = 1.12 s, (e) t = 1.32 s, (f) t = 1.52 s [7].

CHAPTER 3. METHODOLOGY

There are already many research works on the arc plasma simulation and the metal anode melting. However, the high current used in industrial leads extremely high temperature and velocity in a real EAF. A few researchers investigated the heat transfer from a DC arc plasma to the molten bath in DC electric arc furnace but the melting phenomenon was not taken into account [21-22]. Therefore, in order to develop a comprehensive arc-metal heat transfer model, the research on the plasma arc welding was introduced. Because the plasma arc welding has the very similar heat transfer mechanism and metal melting phenomenon with the scrap melting in EAF, the research works [7,17,18] on the plasma arc weld field was referred to help the model development.

In order to correctly simulate the plasma arc and its heat transfer with the anode, the free-burning arc model was developed first. Afterwards, the arc-metal heat transfer model was coupled with the free-burning arc model to predict melting phenomenon of the anode. Figure 14 shows the flow chart of the simulation process and details about the process are described below:

1. In order to understand the arc discharging phenomenon and the mechanism behind it, this study starts with a baseline case for the 2D DC electric arc model. The validated arc model is able to predict the bell shape of the arc as well as the distribution of the arc temperature and the arc velocity.

2. The 2D arc model is enhanced to 3D arc model in order to investigate the model feasibility and applicability and prepare for further application. The 3D arc model is validated with the validated 2D arc model.

3. A baseline case for the 2D arc-metal heat transfer model is established and coupled with the arc model. The integrated model is validated with the experimental data. The validated arc-metal heat transfer model captures the melting profile of the molten pool in the anode as well as the temperature distribution of the anode. In addition, the variation of the arc profile during the melting process is also predicted.

4. Based on the developed DC electric arc model, some interested parameters are further investigated in order to evaluate the impact factor for the arc model. The impact factors investigated in this study are listed below:

    I.   Current quantity

II.   Metal initial temperature
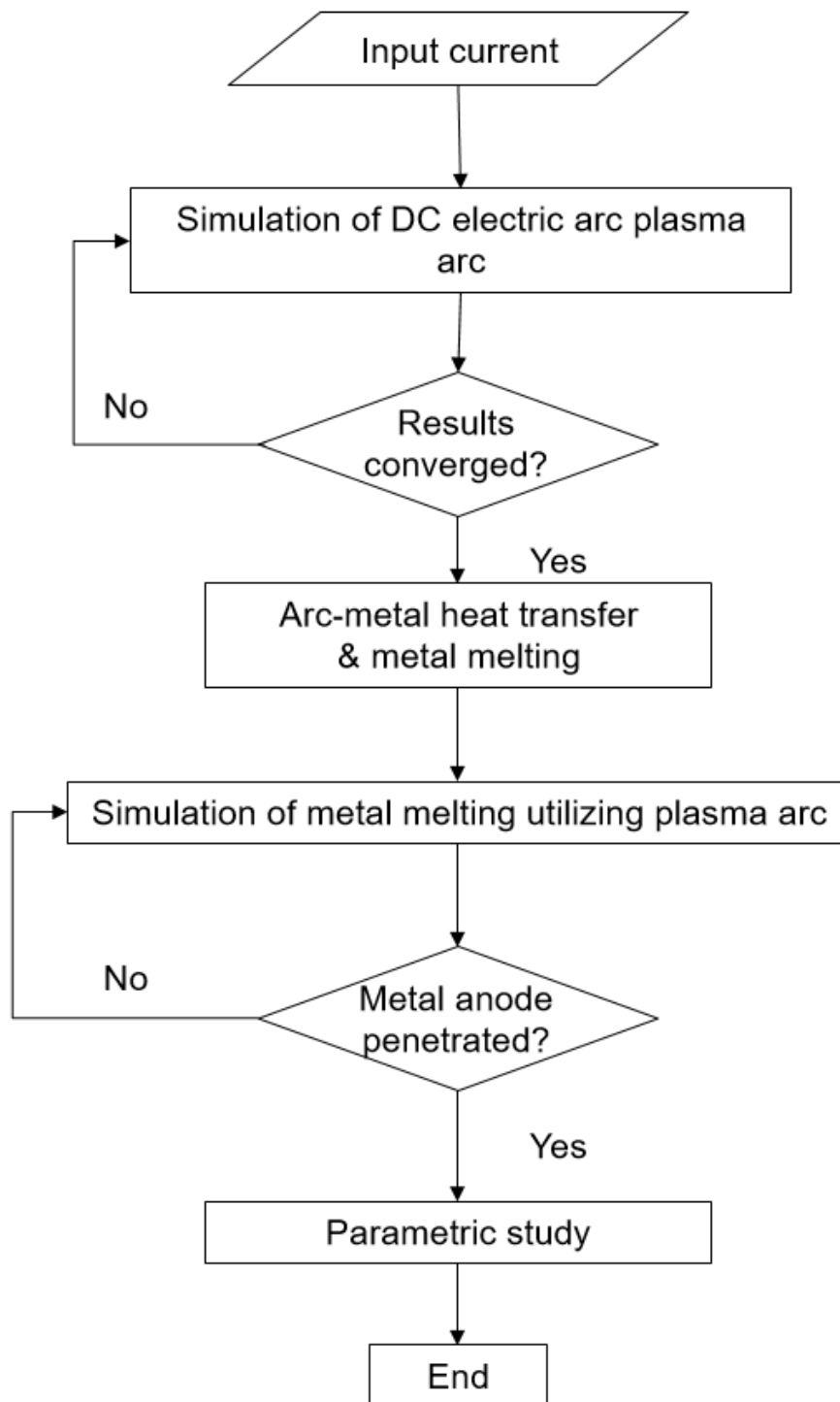
Figure 14. Flow chart of the simulation process.

CHAPTER 4. MODELING OF THE DC ELECTRIC ARC

The DC electric arc model was established to capture the temperature and velocity distribution of a DC electric arc, which was the first step to develop the arc-metal heat transfer model. A 2D model and a 3D model were both constructed and compared. Furthermore, the simulation results were validated with the experimental data.

4.1 Simulation Assumptions

According to the results of literature review [8, 11], several common assumptions for this kind of simulation were made:

1) The arc is optically thin and in LTE.
2) The arc flow is incompressible Newtonian fluid, steady state and laminar.
3) The effects of gravity and heat dissipation due to the viscosity are neglected.
4) The arc is axisymmetric in the 2D configuration.

4.2 Numerical Models

4.2.1 Governing Equations for Two-dimensional Model

The magneto hydrodynamics (MHD) theory was applied to develop the DC electric arc model, which was coupled the Navier-Stokes equation of fluid dynamics and the Maxwell's equations of electromagnetism. The 2D model was developed based on the cylindrical coordinates. Therefore, the conservation equations may be written as:

Mass conservation equation:

$$\frac{\partial(\rho u)}{\partial x} + \frac{1}{r}\frac{\partial(\rho r v)}{\partial r} = 0 \qquad [\,12\,]$$

where ρ is the density, u and v is the axial and radial velocity, respectively.

Axial momentum conservation equation:

$$\rho u \frac{\partial u}{\partial x} + \rho v \frac{\partial u}{\partial r} = -\frac{\partial p}{\partial x} + 2\frac{\partial}{\partial x}\left(\frac{\mu \partial u}{\partial x}\right) + \frac{1}{r}\frac{\partial}{\partial r}\left(\mu r \frac{\partial u}{\partial r}\right) + \frac{1}{r}\frac{\partial}{\partial r}\left(\mu r \frac{\partial v}{\partial x}\right) + j_r B_\theta \qquad [\,13\,]$$

Radial momentum conservation equation:

$$\rho u \frac{\partial v}{\partial x} + \rho v \frac{\partial v}{\partial r} = -\frac{\partial p}{\partial r} + \frac{\partial}{\partial x}\left(\mu \frac{\partial v}{\partial x}\right) + \frac{2}{r}\frac{\partial}{\partial r}\left(\mu r \frac{\partial v}{\partial r}\right) + \frac{\partial}{\partial x}\left(\mu \frac{\partial u}{\partial r}\right) - \frac{2\mu v}{r^2} - j_x B_\theta \qquad [\,14\,]$$

where μ is viscosity, j_r, j_x and B_θ is radial and axial current density component and azimuthal magnetic induction, respectively.

Energy conservation equation:

$$\rho u c_p \frac{\partial T}{\partial x} + \rho v c_p \frac{\partial T}{\partial r} = \frac{\partial}{\partial x}\left(k \frac{\partial T}{\partial x}\right) + \frac{1}{r}\frac{\partial}{\partial r}\left(kr \frac{\partial T}{\partial r}\right) + \frac{j_x^2 + j_r^2}{\sigma} + \frac{5}{2}\frac{K_B}{e}\left(j_x \frac{\partial T}{\partial x} + j_r \frac{\partial T}{\partial r}\right) - S_r \quad [\,15\,]$$

where c_p is the specific heat, T is the temperature, k is the thermal conductivity, σ is the electric conductivity, K_B is the Boltzmann constant, e is the elementary electric charge, S_r is the radiation heat loss.

Current continuity equation:

$$\frac{1}{r}\frac{\partial}{\partial r}\left(\sigma r \frac{\partial V}{\partial r}\right) + \frac{\partial}{\partial x}\left(\sigma \frac{\partial V}{\partial x}\right) = 0 \qquad\qquad [\,16\,]$$

where V is the electrical potential.

Axial vector potential equation:

$$\frac{1}{r}\frac{\partial}{\partial r}\left(r \frac{\partial A_x}{\partial r}\right) + \frac{\partial}{\partial x}\left(\frac{\partial A_x}{\partial x}\right) = -\mu_0 j_x \qquad\qquad [\,17\,]$$

Radial vector potential equation:

$$\frac{1}{r}\frac{\partial}{\partial r}\left(r \frac{\partial A_r}{\partial r}\right) + \frac{\partial}{\partial x}\left(\frac{\partial A_r}{\partial x}\right) = -\mu_0 j_r + \frac{A_r}{r^2} \qquad\qquad [\,18\,]$$

where μ_0 is the magnetic permeability.

Azimuthal magnetic induction:

$$\vec{B} = \vec{\nabla} \times \vec{A} \qquad\qquad [\,19\,]$$

$$B_\theta = \frac{\partial A_r}{\partial x} - \frac{\partial A_x}{\partial r} \qquad\qquad [\,20\,]$$

Current density components:

$$j_x = -\sigma \frac{\partial V}{\partial x} \qquad [\,21\,]$$

$$j_r = -\sigma \frac{\partial V}{\partial r} \qquad [\,22\,]$$

4.2.2 Governing Equations for Three-dimensional Model

Mass conservation equation:

$$\vec{\nabla} \cdot (\rho \vec{v}) = 0 \qquad [\,23\,]$$

where $\vec{v}$ is the velocity vector.

X momentum conservation equation:

$$\vec{\nabla} \cdot (\rho \vec{v} u) = \vec{\nabla} \cdot (\mu \vec{\nabla} u) - \frac{\partial P}{\partial x} + \frac{\partial}{\partial x}\left[\mu \left(2\frac{\partial u}{\partial x} - \frac{2}{3}\vec{\nabla} \cdot \vec{v}\right)\right]$$
$$+ \frac{\partial}{\partial y}\left[\mu\left(\frac{\partial u}{\partial y} + \frac{\partial v}{\partial x}\right)\right] + \frac{\partial}{\partial z}\left[\mu\left(\frac{\partial u}{\partial z} + \frac{\partial w}{\partial x}\right)\right] + j_y \cdot B_z - j_z \cdot B_y \qquad [\,24\,]$$

Y momentum conservation equation:

$$\vec{\nabla} \cdot (\rho \vec{v} v) = \vec{\nabla} \cdot (\mu \vec{\nabla} v) - \frac{\partial P}{\partial y} + \frac{\partial}{\partial y}\left[\mu \left(2\frac{\partial u}{\partial y} - \frac{2}{3}\vec{\nabla} \cdot \vec{v}\right)\right]$$
$$+ \frac{\partial}{\partial x}\left[\mu\left(\frac{\partial v}{\partial x} + \frac{\partial u}{\partial y}\right)\right] + \frac{\partial}{\partial z}\left[\mu\left(\frac{\partial v}{\partial z} + \frac{\partial w}{\partial y}\right)\right] + j_z \cdot B_x - j_x \cdot B_z \qquad [\,25\,]$$

Z momentum conservation equation:

$$\vec{\nabla} \cdot (\rho \vec{v} w) = \vec{\nabla} \cdot (\mu \vec{\nabla} w) - \frac{\partial P}{\partial z} + \frac{\partial}{\partial z}\left[\mu \left(2\frac{\partial w}{\partial z} - \frac{2}{3}\vec{\nabla} \cdot \vec{v}\right)\right]$$
$$+ \frac{\partial}{\partial x}\left[\mu\left(\frac{\partial w}{\partial x} + \frac{\partial u}{\partial z}\right)\right] + \frac{\partial}{\partial y}\left[\mu\left(\frac{\partial w}{\partial y} + \frac{\partial v}{\partial z}\right)\right] + j_x \cdot B_y - j_y \cdot B_x \qquad [\,26\,]$$

Energy conservation equation:

$$\vec{\nabla} \cdot (\rho \vec{v} T) = \vec{\nabla} \cdot \left(\frac{k}{c_p}\vec{\nabla} T\right) + \frac{j_x^2 + j_y^2 + j_z^2}{\sigma} - S_r + \frac{5}{2}\frac{k_B}{e}\left(\frac{j_x}{C_P}\frac{\partial T}{\partial x} + \frac{j_y}{C_P}\frac{\partial T}{\partial y} + \frac{j_z}{C_P}\frac{\partial T}{\partial z}\right) \qquad [\,27\,]$$

Current continuity equation:

$$\vec{\nabla} \cdot (\rho \vec{v} V) = \vec{\nabla} \cdot (\sigma \vec{\nabla} V) \qquad [\,28\,]$$

X vector potential equation:

$$\vec{\nabla} \cdot (\rho \vec{v} A_x) = \vec{\nabla} \cdot (\vec{\nabla} A_x) + \mu_0 j_x \qquad [\,29\,]$$

Y vector potential equation:

$$\vec{\nabla} \cdot (\rho \vec{v} A_y) = \vec{\nabla} \cdot (\vec{\nabla} A_y) + \mu_0 j_y \qquad [\,30\,]$$

Z vector potential equation:

$$\vec{\nabla} \cdot (\rho \vec{v} A_z) = \vec{\nabla} \cdot (\vec{\nabla} A_z) + \mu_0 j_z \qquad [\,31\,]$$

Azimuthal magnetic induction:

$$\vec{B} = \vec{\nabla} \times \vec{A} \qquad [\,32\,]$$

$$B_x = \frac{\partial A_z}{\partial y} - \frac{\partial A_y}{\partial z} \qquad [\,33\,]$$

$$B_y = \frac{\partial A_x}{\partial z} - \frac{\partial A_z}{\partial x} \qquad [\,34\,]$$

$$B_z = \frac{\partial A_y}{\partial x} - \frac{\partial A_x}{\partial y} \qquad [\,35\,]$$

Current density components:

$$j_x = -\sigma \frac{\partial V}{\partial x} \qquad [\,36\,]$$

$$j_y = -\sigma \frac{\partial V}{\partial y} \qquad [\,37\,]$$

$$j_z = -\sigma \frac{\partial V}{\partial z} \qquad [\,38\,]$$

4.3 Computational Domain

4.3.1 2D Computational Domain Configuration

According to the research work done by Lago el at. [11], the 2D computational domain was developed for this simulation. As shown in Figure 15, the computational domain of 15×13 mm^2 is represented in a cylindrical coordinate. The mesh is refined near the axis and cathode tip. This 2D configuration is consisted of free gas region and tungsten cathode walls with a $60°$ angle tip and a height of 3 mm.
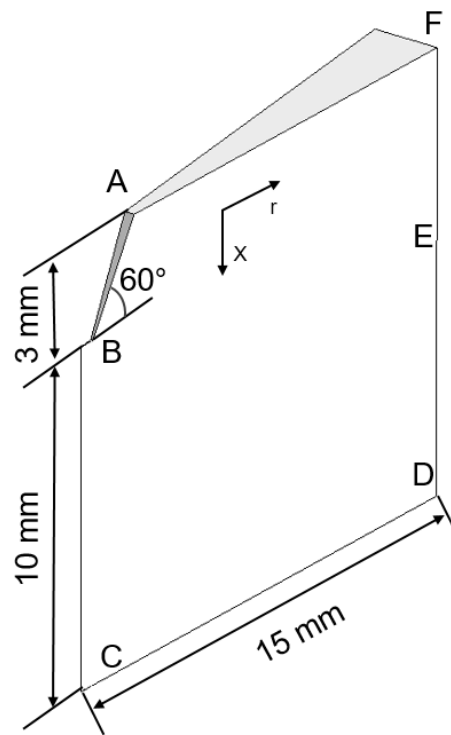
Figure 15. Computational domain for 2D DC electric arc model

4.3.2 3D Computational Domain Configuration

The 3D computational domain was developed based on the 2D computational domain, which basically had the same configuration shown in Figure 16.

35
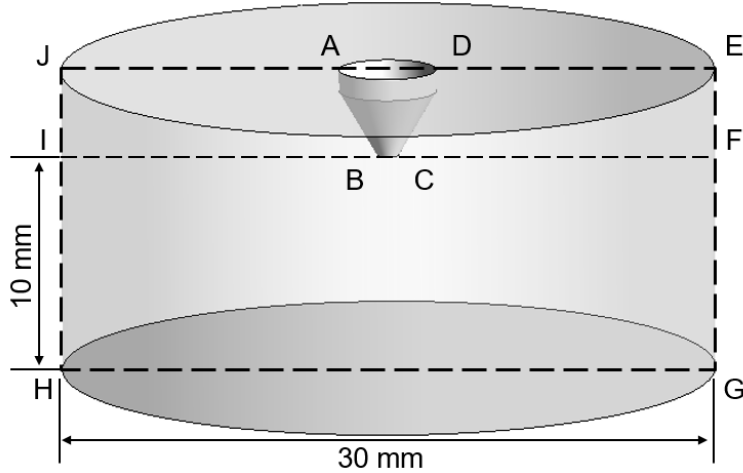
Figure 16. Computational domain for 3D DC electric arc model

4.4 Boundary Condition

The current used in this simulation is 200A and the medium is at atmospheric pressure for both 2D and 3D simulation. Only the arc column was simulated in this section. The boundary conditions for the 2D and 3D simulation was indexed in Table 1 and Table 2, respectively. The current distribution at the cathode tip (BE, IF) was assumed to be equation (6).

Table 1. Typical boundary conditions for a 2D free-burning arc.

	BC	CD	DF	AF	AB	BE
u	$\dfrac{\partial u}{\partial r} = 0$	$u = 0$	$u = 0$	$\dfrac{\partial \rho u}{\partial r} = 0$	$u = 0$	-
v	$v = 0$	$v = 0$	$\dfrac{\partial \rho v}{\partial r} = 0$	$v = 0$	$v = 0$	-
T	$\dfrac{\partial T}{\partial r} = 0$	$\dfrac{\partial T}{\partial x} = 0$	$T = 1000\text{K}$	$T = 1000\text{K}$	$T = 3500\text{K}$	-
V	$\dfrac{\partial V}{\partial r} = 0$	$V = 0$	$\dfrac{\partial V}{\partial r} = 0$	$\dfrac{\partial V}{\partial r} = 0$	-	Eq. (6)

36

Table 2. Typical boundary conditions for a 3D free-burning arc.

	AB, BC, CD	JA, DE	EF, FG, JI, IH	HG	FI
u	$u = 0$	$u = 0$	$u = 0$	-	-
v	$v = 0$	$v = 0$	$\dfrac{\partial \rho v}{\partial y} = 0$	$v = 0$	-
w	$w = 0$	$\dfrac{\partial \rho w}{\partial z} = 0$	$w = 0$	$w = 0$	-
T	$T = 3500$ K	$T = 1000$ K	$T = 1000$ K	$\dfrac{\partial T}{\partial z} = 0$	-
V	$\dfrac{\partial V}{\partial \vec{n}} = 0$	$\dfrac{\partial V}{\partial z} = 0$	$\dfrac{\partial V}{\partial y} = 0$	$V = 0$	Eq. (6)
A_x	$\dfrac{\partial A_x}{\partial \vec{n}} = 0$	$\dfrac{\partial A_x}{\partial z} = 0$	$\dfrac{\partial A_x}{\partial y} = 0$	$\dfrac{\partial A_x}{\partial z} = 0$	-
A_y	$\dfrac{\partial A_y}{\partial \vec{n}} = 0$	$\dfrac{\partial A_y}{\partial z} = 0$	$\dfrac{\partial A_y}{\partial y} = 0$	$\dfrac{\partial A_y}{\partial z} = 0$	-
A_z	$\dfrac{\partial A_z}{\partial \vec{n}} = 0$	$\dfrac{\partial A_z}{\partial z} = 0$	$\dfrac{\partial A_z}{\partial y} = 0$	$\dfrac{\partial A_z}{\partial z} = 0$	-

4.5 Material Properties

Argon was used as the plasma gas in this simulation. The thermal properties of argon, such as density, viscosity, thermal conductivity, specific heat, electrical conductivity, and radiation coefficient are temperature independent and taken from the book [28], which is shown below (Figure 17).
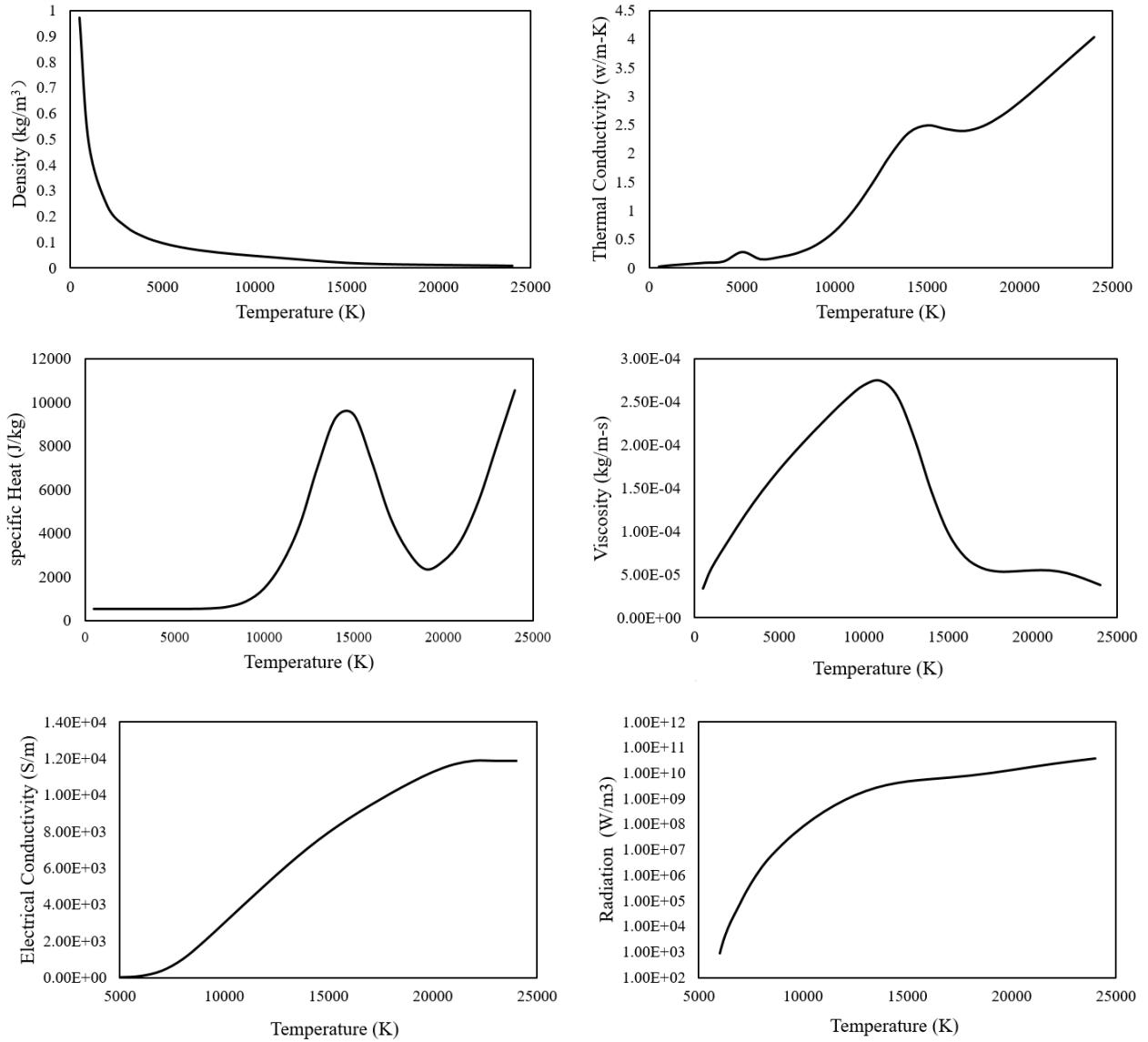
Figure 17. Thermophysical properties of argon plasma for simulation [28].

4.6 Results and Discussion

4.6.1 Model Validation of 2D Simulation

Figure 18 (a) shows the temperature distribution of the free-burning argon plasma arc. A typical bell shape of the arc plasma was obtained, as the strong cathode jet is impinging the metal anode surface and dispersing. For a 200-A-current arc, the highest temperature is able to reach 22000 K below the electrode tip. The middle of the arc column maintains a high temperature above 10000

K. The temperature is spreading from the cathode tip towards the anode. The stronger diffusion of the temperature in radial was observed near the anode surface. Figure 18 (b) shows comparison of the measured and calculated isotherms of the argon arc plasma. The measured data is on the left side, which is from the experimental work conducted by Hsu el at. [8]. The calculated results conducted by this study are on the right side. With the comparison, it is shown that the predicted arc temperature distribution was in fairly good agreement with the experimental data. It is also observed that along the arc column centerline, the temperature decrease slowly from the cathode tip to the anode surface because of the very high velocity of the cathode jet.

Figure 19 (a) reveals the velocity distribution of the free-burning arc. The cathode jet is very strong and slight diffusion around the jet was observed. The cathode jet is impinging towards the metal anode surface. The middle region in the arc column maintains relatively high velocity. From Figure 19 (b), a clearer tendency of the centerline velocity of the free-burning arc was illustrated. The arc plasma accelerates dramatically from the cathode tip and reaches the maximum velocity at 0.8 mm. Then the arc plasma velocity is decaying smoothly from 0.8 mm to 8.8 mm away from the cathode tip, but a rapid decay is observed after. Figure 19 (b) also shows the predicted axial centerline velocity obtained by other researchers. In Hsu's simulation, the Ampere's law method was used to calculate the self-induced magnetic field B_θ:

$$B_\theta = \frac{\mu_0}{r} \int_0^R j_z(r) r dr \qquad [39]$$

More important values of velocity were obtained using the Ampere's law method than using the potential vector method. However, based on the suggestion by Ramirez el at. [29], the potential vector method can reduce the complexities on the mathematical calculation. Lago el at. [11] also discussed these two methods and concluded that the potential vector approach was superior. Therefore, the potential vector method was applied in the whole arc plasma simulation. It is also shown that the simulation results obtained in this study has a pretty good agreement with results reported by other researchers'. According to the validation on the profile of the plasma arc temperature and velocity, the good agreements indicated the present model for the arc plasma simulation is credible.
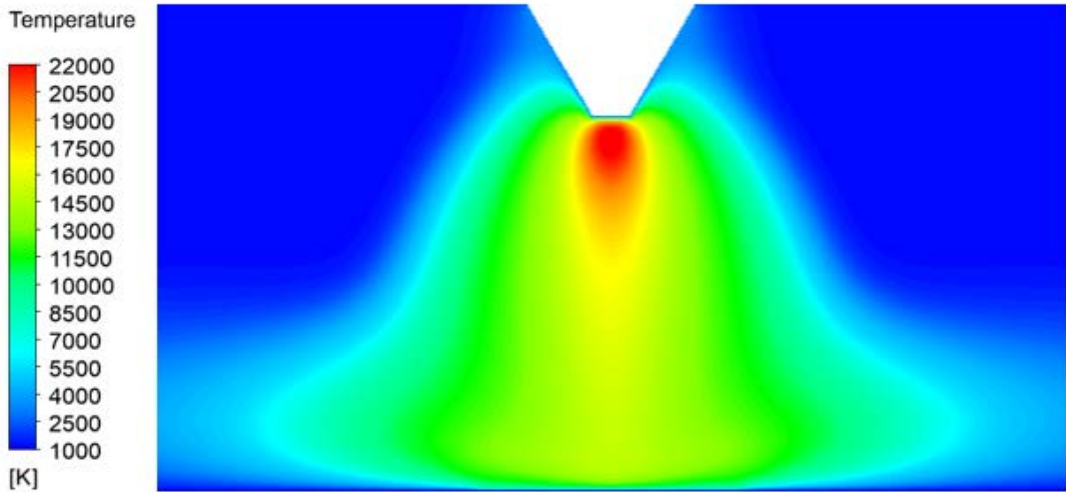
(a)
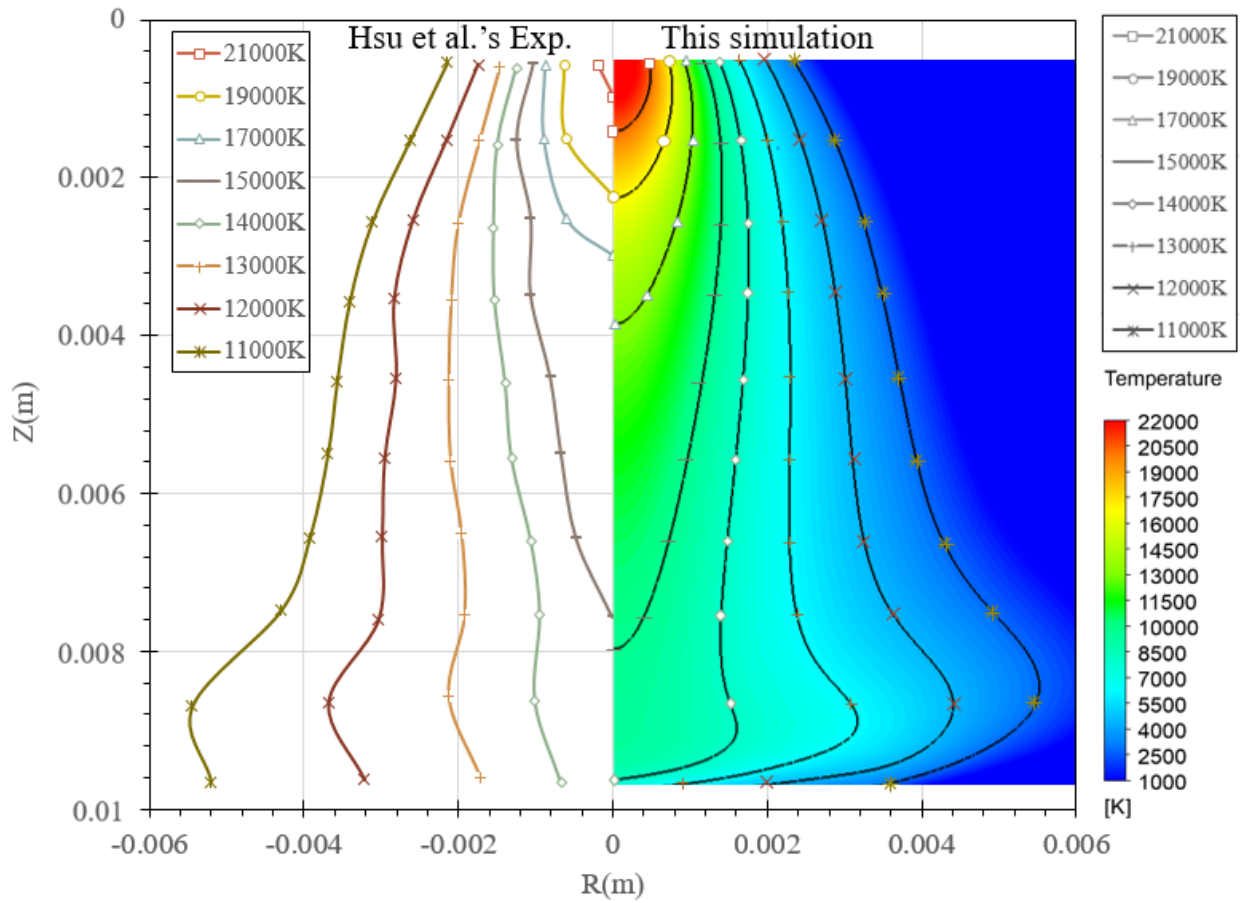
(b)

Figure 18. Temperature contours. (a) Temperature distribution of the DC electric arc.
(b) Comparison of the measured and calculated isotherms of the DC electric argon arc [8].
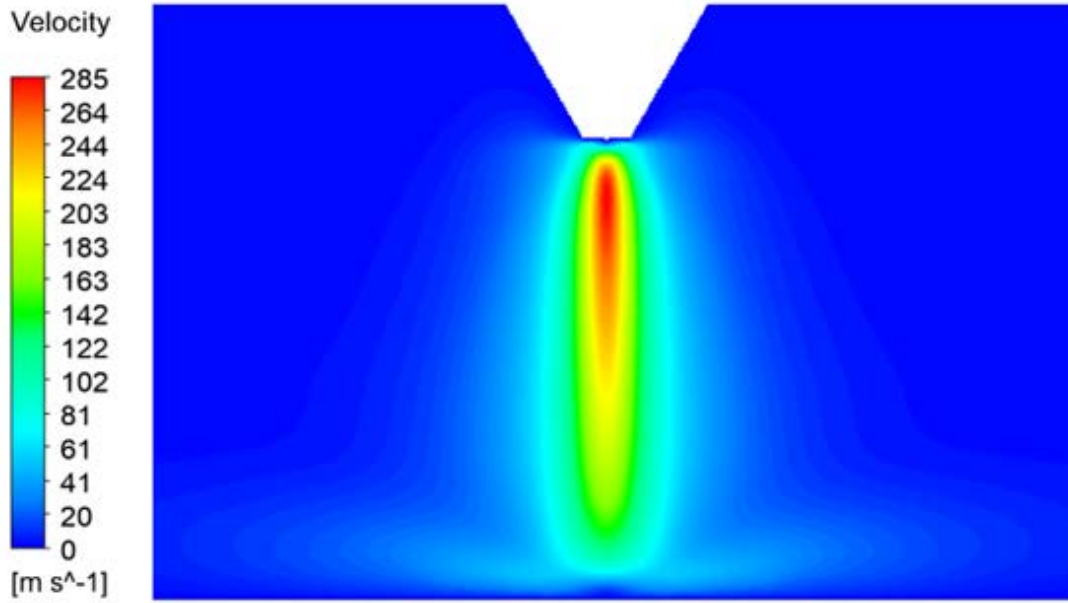
(a)
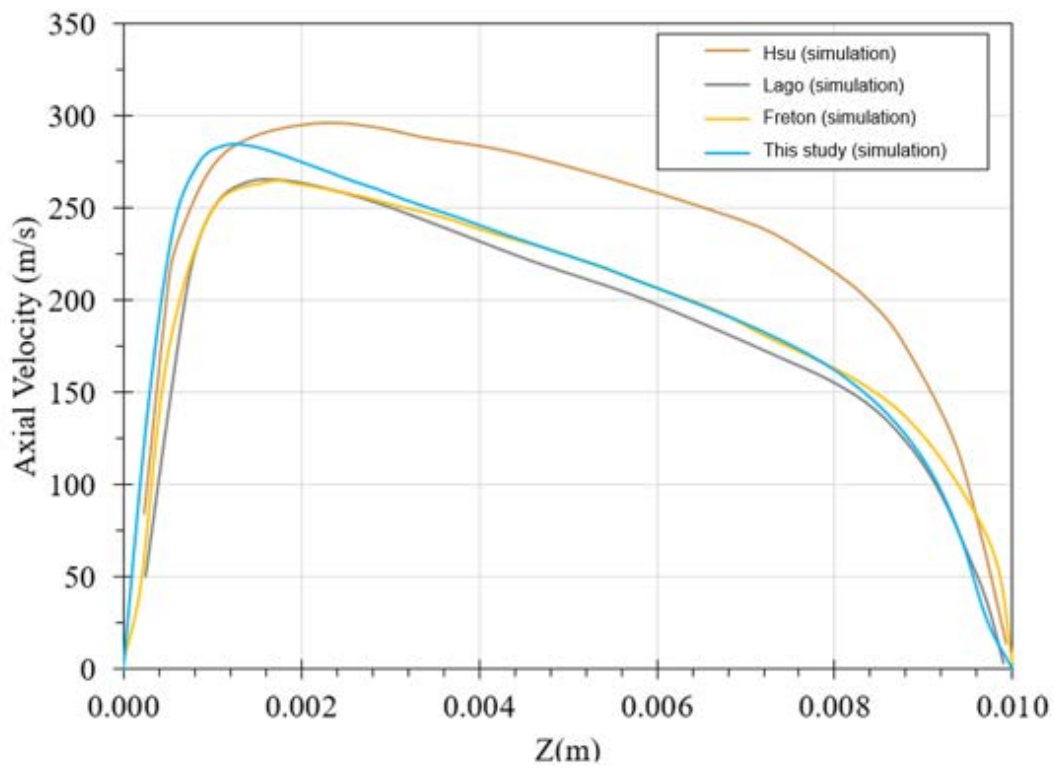
(b)

Figure 19. Velocity profile. (a) Velocity distribution of the DC electric arc. (b) Comparison of the centerline velocity of the DC electric arc [8, 29].

4.6.2 Model Validation of 3D Simulation

To enhance the electric arc model to 3D, the third direction was taken into account. In Figure 20, two temperature profiles were presented for the two-dimensional and the three-dimensional configurations. Because the two-dimensional model has been validated, the three-dimensional simulation results were validated with the two-dimensional simulation results. The typical bell shape was observed in the three-dimensional simulation. Comparing the isotherms in Figure 20, it can be said that the three-dimensional simulation results on temperature have a pretty good agreement with the two-dimensional simulation results.
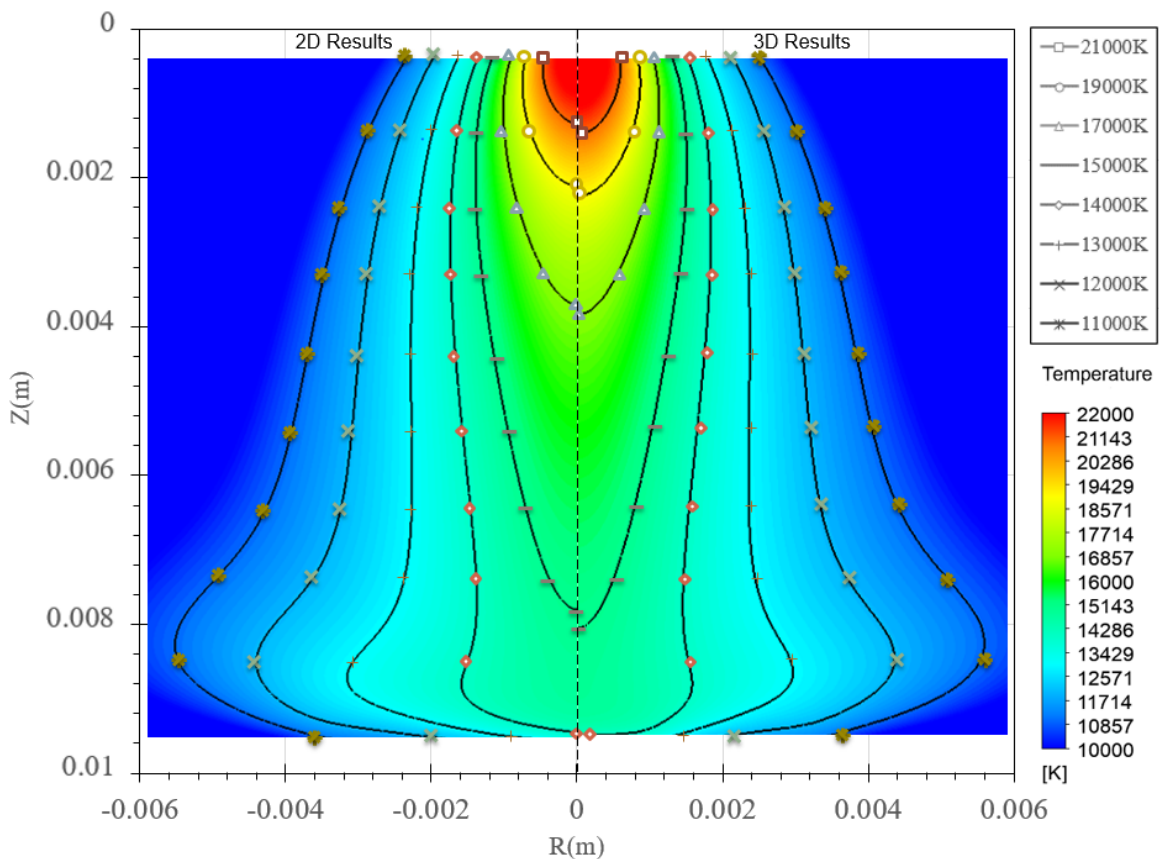
Figure 20. Comparison between the temperature profile in two-dimensional and three-dimensional configurations.

Figure 21 shows the velocity distribution of the free-burning arc plasma at the axial centerline for the two-dimensional and the three-dimensional configurations. Basically, the same distribution of the axial centerline velocity for three-dimensional simulation as the two-dimensional simulation

was obtained. It can be said the three-dimensional free-burning arc plasma model was validated and the results were pretty reliable.
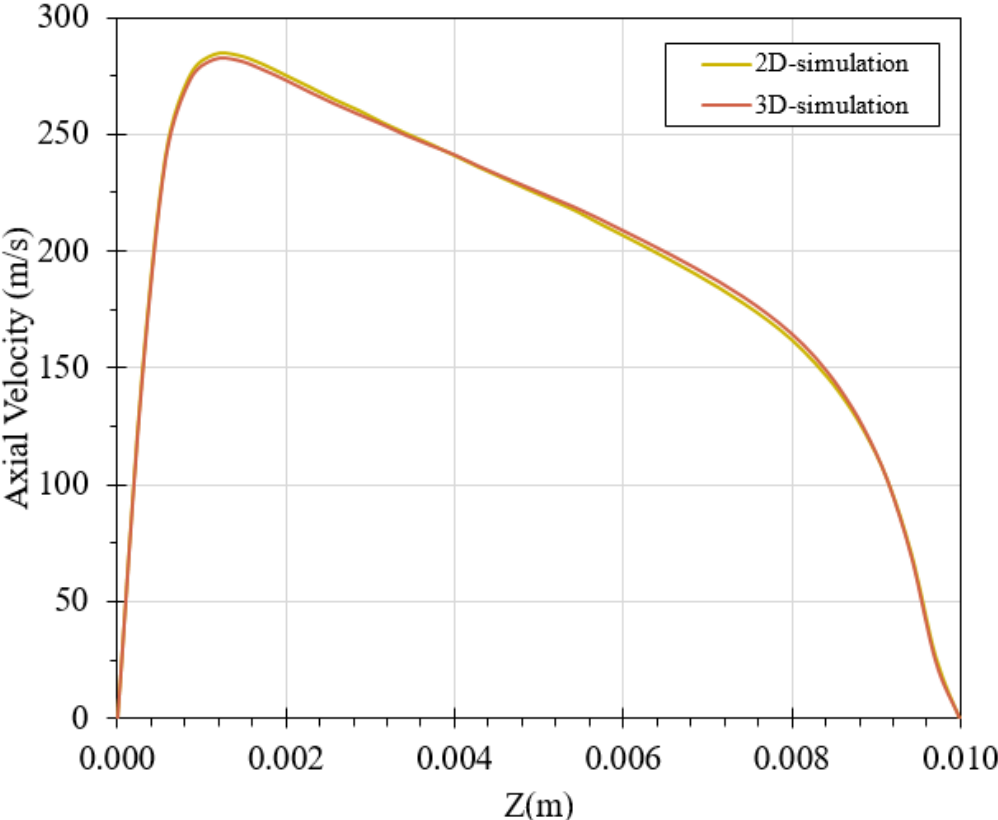
Figure 21. Comparison between the velocity profile in two-dimensional and three-dimensional configurations.

CHAPTER 5. MODELING OF THE METAL MELTING PROCESS UTILIZING A DC ELECTRIC ARC PLASMA

5.1 Simulation Assumptions

According to other researcher's work [7, 17], several assumptions were made:

1) The arc is optically thin and in LTE.
2) The fluids are incompressible.
3) The flow of arc and molten pool are turbulent.
4) The arc is axisymmetric.
5) The metal vaporization is ignored.

5.2 Numerical Models

5.2.1 Governing Equations

Mass conservation equation:

$$\frac{\partial \rho}{\partial t} + \frac{\partial(\rho u)}{\partial x} + \frac{1}{r}\frac{\partial(\rho r v)}{\partial r} = 0 \qquad [\,40\,]$$

Axial momentum conservation equation:

$$\frac{\partial \rho u}{\partial t} + \rho u \frac{\partial u}{\partial x} + \rho v \frac{\partial u}{\partial r} = -\frac{\partial p}{\partial x} + 2\frac{\partial}{\partial x}\left(\frac{\mu \partial u}{\partial x}\right) + \frac{1}{r}\frac{\partial}{\partial r}\left(\mu r \frac{\partial u}{\partial r}\right) + \frac{1}{r}\frac{\partial}{\partial r}\left(\mu r \frac{\partial v}{\partial x}\right) + S_m \qquad [\,41\,]$$

$$S_m^{arc} = j_r B_\theta \qquad [\,42\,]$$

$$S_m^{anode} = j_r B_\theta + \rho g \beta (T - T_r) \qquad [\,43\,]$$

where β is thermal expansion coefficient, T_r is the reference temperature.

Radial momentum conservation equation:

$$\frac{\partial \rho v}{\partial t} + \rho u \frac{\partial v}{\partial x} + \rho v \frac{\partial v}{\partial r} = -\frac{\partial p}{\partial r} + \frac{\partial}{\partial x}\left(\mu \frac{\partial v}{\partial x}\right) + \frac{2}{r}\frac{\partial}{\partial r}\left(\mu r \frac{\partial v}{\partial r}\right) + \frac{\partial}{\partial x}\left(\mu \frac{\partial u}{\partial r}\right) - \frac{2\mu v}{r^2} - j_x B_\theta \quad [\,44\,]$$

Energy conservation equation:

$$\frac{\partial \rho h}{\partial t} + \frac{1}{r}\frac{\partial}{\partial r}(r\rho vh) + \frac{\partial}{\partial x}(\rho uh) = \frac{1}{r}\frac{\partial}{\partial r}\left(\frac{rk}{C_P}\frac{\partial h}{\partial r}\right) + \frac{\partial}{\partial x}\left(\frac{k}{C_P}\frac{\partial h}{\partial x}\right) + S_h \qquad [\,45\,]$$

$$S_h^{arc} = \frac{J_z^2 + J_r^2}{\sigma} + \frac{5}{2}\frac{K_b}{e}\left(\frac{J_z}{C_P}\frac{\partial h}{\partial x} + \frac{J_r}{C_P}\frac{\partial h}{\partial r}\right) - S_r \qquad [\,46\,]$$

$$S_h^{andoe} = \frac{J_z^2 + J_r^2}{\sigma} \qquad [\,47\,]$$

Current continuity equation:

$$\frac{1}{r}\frac{\partial}{\partial r}\left(\sigma r\frac{\partial V}{\partial r}\right) + \frac{\partial}{\partial x}\left(\sigma\frac{\partial V}{\partial x}\right) = 0 \qquad [\,48\,]$$

Axial vector potential equation:

$$\frac{1}{r}\frac{\partial}{\partial r}\left(r\frac{\partial A_x}{\partial r}\right) + \frac{\partial}{\partial x}\left(\frac{\partial A_x}{\partial x}\right) = -\mu_0 j_x \qquad [\,49\,]$$

Radial vector potential equation:

$$\frac{1}{r}\frac{\partial}{\partial r}\left(r\frac{\partial A_r}{\partial r}\right) + \frac{\partial}{\partial x}\left(\frac{\partial A_r}{\partial x}\right) = -\mu_0 j_r + \frac{A_r}{r^2} \qquad [\,50\,]$$

Azimuthal magnetic induction:

$$\vec{B} = \vec{\nabla} \times \vec{A} \qquad [\,51\,]$$

$$B_\theta = \frac{\partial A_r}{\partial x} - \frac{\partial A_x}{\partial r} \qquad [\,52\,]$$

Current density components:

$$j_x = -\sigma\frac{\partial V}{\partial x} \qquad [\,53\,]$$

$$j_r = -\sigma\frac{\partial V}{\partial r} \qquad [\,54\,]$$

5.2.2 Turbulence Model

In order to take the effect of the turbulent flow into account, the standard k-ε model [7,23,24] was used to determine the turbulence kinetic energy k and the its rate of dissipation ε.

The turbulence kinetic energy k and the turbulence dissipation rate were expressed as:

$$\frac{\partial}{\partial t}(\rho k) + \frac{\partial}{\partial x_i}(\rho k u_i) = \frac{\partial}{\partial x_j}\left[\left(\mu + \frac{\mu_t}{\sigma_k}\right)\frac{\partial k}{\partial x_j}\right] + G_k + G_b - \rho\varepsilon - Y_M + S_K \qquad [55]$$

$$\frac{\partial}{\partial t}(\rho\varepsilon) + \frac{\partial}{\partial x_i}(\rho\varepsilon u_i) = \frac{\partial}{\partial x_j}\left[\left(\mu + \frac{\mu_t}{\sigma_\varepsilon}\right)\frac{\partial\varepsilon}{\partial x_j}\right] + C_{1\varepsilon}\frac{\varepsilon}{k}(G_k + C_{3\varepsilon}G_b) - C_{2\varepsilon}\rho\frac{\varepsilon^2}{k} + S_\varepsilon \qquad [56]$$

The turbulence viscosity was obtained by:

$$\mu_t = c_\mu\rho\frac{k^2}{\varepsilon} \qquad [57]$$

where G_k is the generation of turbulence kinetic energy due to the mean velocity gradients, G_b represents the generation of turbulence kinetic energy due to buoyancy, Y_M is the contribution of the fluctuating dilatation in compressible turbulence to the overall dissipation rate, $C_{1\varepsilon}$, $C_{2\varepsilon}$, c_μ, σ_k and σ_ε are constant, which are 1.44, 1.92, 0.09, 1.0 and 1.3, respectively.

5.2.3 Solidification and Melting Model

The enthalpy-porosity technique was applied to deal with the mushy zone. The fluid was assumed to be porous medium. The liquid fraction β of the fluid is defined as:

$$\beta = \begin{cases} 0 & T < T_{solidus} \\ \dfrac{T - T_{solidus}}{T_{liquidus} - T_{solidus}} & T_{solidus} < T < T_{liquidus} \\ 1 & T > T_{liquidus} \end{cases} \qquad [58]$$

An additional energy source term is added to the energy equation:

$$S = \Delta H\frac{\partial\beta}{\partial t} \qquad [59]$$

where ΔH is the latent heat.

An additional source term is added to the axial and radial momentum equations:

$$S = A_{mush} \frac{(1-\beta)^2}{\beta^3 + \xi} (\vec{v} - \vec{v_p})$$ [60]

where A_{mush} is the mushy zone constant, ξ is a small number to prevent division by zero, $\vec{v_p}$ is the solid velocity because of the pulling of solidified material out of the domain.

Additional source terms are added to all of the turbulence equations in the mushy zones:

$$S = A_{mush} \frac{(1-\beta)^2}{\beta^3 + \xi} \emptyset$$ [61]

where $\emptyset$ is the turbulence quantity being solved (k & ε).

5.2.4 Interface Tracking

In this study, with the heat transfer from the arc plasma to the metal, the metal was heated and molten pool was formed. Under the effect of the arc pressure, the molten pool starts to deform and the plasma flow finally penetrates the work piece. During this process, a free interface between the arc and molten pool was formed and the heat transfer between the arc and metal will be impacted due to the free interface. Therefore, capturing the free interface between the arc and metal is a key to implement the arc-metal heat transfer. The VOF method is applied to track the dynamic interface between arc and scrap in this numerical simulation [7, 17]. The volume of fluid fraction F for a cell is determined by the function:

$$\frac{dF}{dt} + \frac{1}{r}\frac{\partial}{\partial r}(rv_r F) + \frac{\partial}{\partial x}(v_x F) = 0$$ [62]

5.2.5 Arc-metal Heat Transfer

Based on the arc-metal heat transfer mechanism, the total heat flux at the metal anode surface included electronic heat, conductive heat, and radiation loss [7, 26]. However, the metal vaporization at the anode surface was ignored in this study [25]. Therefore, the additional energy source term added in the anode interface was:

$$S_{anode} = |J|\varphi_a + \frac{k_{eff}(T_{e,a} - T_a)}{\delta} - \varepsilon K_B T_a^4$$ [63]

The additional energy source term added in the plasma arc interface was:

$$S_{arc} = -\frac{k_{eff}(T_{e,a} - T_a)}{\delta} \qquad [\,64\,]$$

where J is the current density, φ_a is the work function of the metal anode, k_{eff} is the effective thermal conductivity [26], $T_{e,a}$ is the arc temperature at the anode interface, T_a is the anode temperature, δ is the thickness of the anode interface, which is taking 0.15 mm [7].

5.3 Computational Domain

Figure 22 shows the computational domain used in this simulation [17]. This is a stationary and axisymmetric welding torch. The IH, FD and DQ are the plasma gas inlet, shielding gas inlet and outlet, respectively. The cathode and nozzle part are not included in this simulation. AC is the axis and the rest was set as wall boundary. BQ is the initial interface between the plasma arc and the metal anode. However, when the metal anode melts, a new free interface between the plasma arc and anode forms and is tracked by using VOF method.
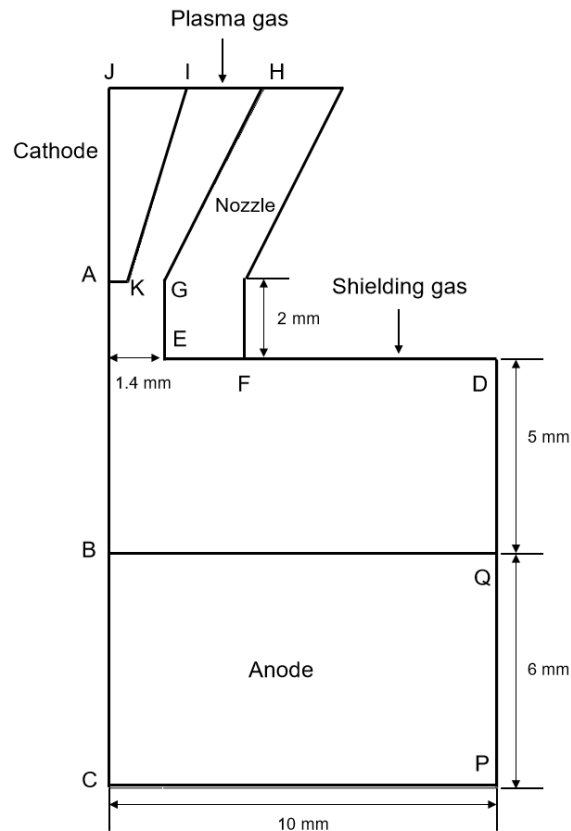
Figure 22. Schematic illustration of the simulation domain.

5.4 Material Properties

The plasma gas is also the argon which is corresponding to the arc simulation in chapter 4. The metal anode material is the stainless steel SUS304. The thermal properties of the stainless steel SUS304, such as density, viscosity, thermal conductivity, specific heat, and electrical conductivity are listed in Table 3.

Table 3. The thermal properties of the stainless steel SUS304 [17].

Density (kg/m^3)	7200
Specific Heat (J/kg·K)	$438.95 + 0.198 \times T$ (T ≤ 773 K)
	$137.93 + 0.59 \times T$ (773 K < T ≤ 873 K)
	$871.25 - 0.25 \times T$ (873 K < T ≤ 973 K)
	$555.2 + 0.0775 \times T$ (T > 973 K)
Solid Temperature (K)	1670
Liquid Temperature (K)	1727
Latent Heat (J/kg)	2.45×10^5
Electric Conductivity (S/m)	770000
Thermal Conductivity (W/m·K)	$10.717 + 0.014955 \times T$ (T < 1672 K)
	$217.12 - 0.1094 \times T$ (1672 < T ≤ 1727)
	$8.278 + 0.0115 \times T$ (T > 1727)
Viscosity (kg/m·s)	$(37.203 - 0.0176 * T) * 1E\text{-}3$ (1713 ≤ T ≤ 1873)
Work function	4.65 V

5.5 Boundary Conditions

Table 4 presents the detailed boundary conditions. The initial temperature of the metal anode is 300K. The current density at the electrode tip is assumed to be uniform. Some important process parameters in this simulation are listed in Table 5.

Table 4. Detailed boundary conditions used in this simulation [17].

	u (m/s)	v (m/s)	T (K)	V
ABC	$\frac{\partial u}{\partial \vec{n}} = 0$	$\frac{\partial v}{\partial \vec{n}} = 0$	$\frac{\partial T}{\partial \vec{n}} = 0$	$\frac{\partial V}{\partial \vec{n}} = 0$
CP	-	-	$k\nabla T - \varepsilon\alpha T^4$	0
PQ	-	-	$k\nabla T - \varepsilon\alpha T^4$	0
QD	-	-	1000	$\frac{\partial V}{\partial \vec{n}} = 0$
DF	Constant	0	1000	$\frac{\partial V}{\partial \vec{n}} = 0$
FEGH	-	-	$k\nabla T$	$\frac{\partial V}{\partial \vec{n}} = 0$
HI	Constant	0	1000	$\frac{\partial V}{\partial \vec{n}} = 0$
IK	-	-	1000	$\frac{\partial V}{\partial \vec{n}} = 0$
KA	-	-	3000	j

Table 5. Main process parameters [17].

Current	170 A
Plasma gas flow rate	3 L/min
Shielding gas flow rate	20 L/min
Thickness of the anode	6 mm
Electrode setback	2 mm

5.6 Model Validation

In order to validate the arc-metal heat transfer model, the computational results are compared with the experimental measurements and other researchers' work. Figure 23 shows the evolution process of the metal anode melted by the arc plasma at different time. During the penetration of the anode by the plasma arc, the shape of the arc plasma varies as anode melts and its surface deforms. Since the plasma jet maintains very high velocity, the impingement on the anode surface is very intense. Therefore, the melted metal anode will get a lot of chances to splash, which might impact the temperature profile of the anode. At the time of 0.1 s, the typical bell shape of the plasma arc is observed and the anode surface is flat. But the anode has been heated by the plasma arc and the very central region of the top surface of the anode has begun melting. At the time of 0.5 s, the anode has been melted and penetrated a lot. As we can see, the shape arc plasma is no longer in a typical bell shape. The plasma jet was impinging on the anode top surface and the high temperature began spreading from the center to the sides. In the anode region, the higher temperature occurred at the anode-arc interface and was conducted to the rest of the anode, although most part of the anode is very cold. At the time of 1.0 s, the arc plasma was still penetrating the anode and the larger area in the anode was heated. However, it can be observed that the penetration rate became slower compared with the contour at 0.5 s. At the time of 1.48 s, the plasma arc has already fully penetrated the anode, which is in agreement with the simulation results conducted by Jian el at. [17]. In a way, the agreement on the penetration time reveals the validity of this model. The arc shape did not change too much at this time when it is compared

with the arc shape at the previous times. In the anode region, the cold region was small at the bottom corner. The temperature was spreading from the anode-arc interface to the remaining part of the anode.

Based on the experiment conducted by Jian et al. [17], the computational melting profile at the transverse cross-section was compared with the experimental melting profile. Figure 24 shows the comparison between the experimental results by Jian et al. and the computational results from this study. The macrographs of melting are at the left-hand side and the calculated results are at right-hand side. The calculated results are presented by the temperature profile of the anode. The red region, where the temperature is above 1727 K, represents the melted anode and the empty area is the region that is penetrated by the arc plasma. Comparing the calculated melting profile with experimental melting profile, it can be said that the current simulation results are valid to a certain extent. Nonetheless, the predicted melting profile is slightly different from the experimental measurements. The heat source used to melt the anode is the arc plasma; thus, the anode melting was determined by the behavior of the arc plasma. However, because the impingement of the arc plasma on the anode surface causes the splashing of the melted anode, the turbulence has to be taken into consideration in this simulation. Therefore, the flow in the whole computational domain was assumed to be turbulent, including the arc plasma which was predicted by the standard k-ε turbulence model. Furthermore, due to the limitation of the standard k-ε turbulence model, this turbulence model is better at solving the fully turbulent flow. Therefore, in some regions with low Reynolds number, the behavior of the arc plasma predicted in this simulation might not be extremely accurate, which might impact the simulation results. In addition, because the metal vaporization was neglected in this simulation, the influence of the metal gas was not taken into account, which might impact the melting profile of the anode and the accuracy of the current simulation results. Thus, further investigation could be pursued in order to refine the current model and improve the accuracy.
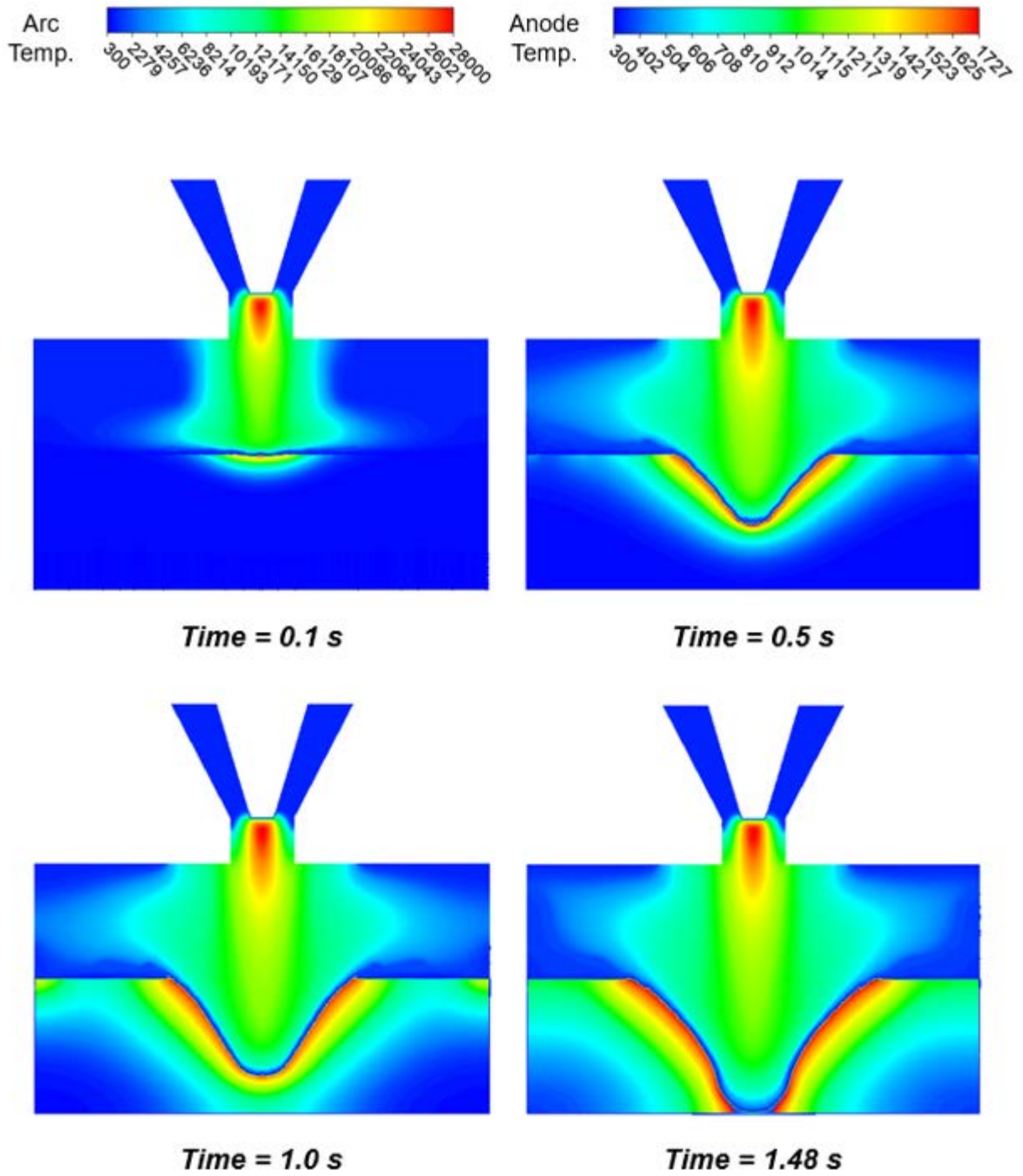
Figure 23. Melting process of the metal anode utilizing the DC electric arc plasma at different times with 170A current.
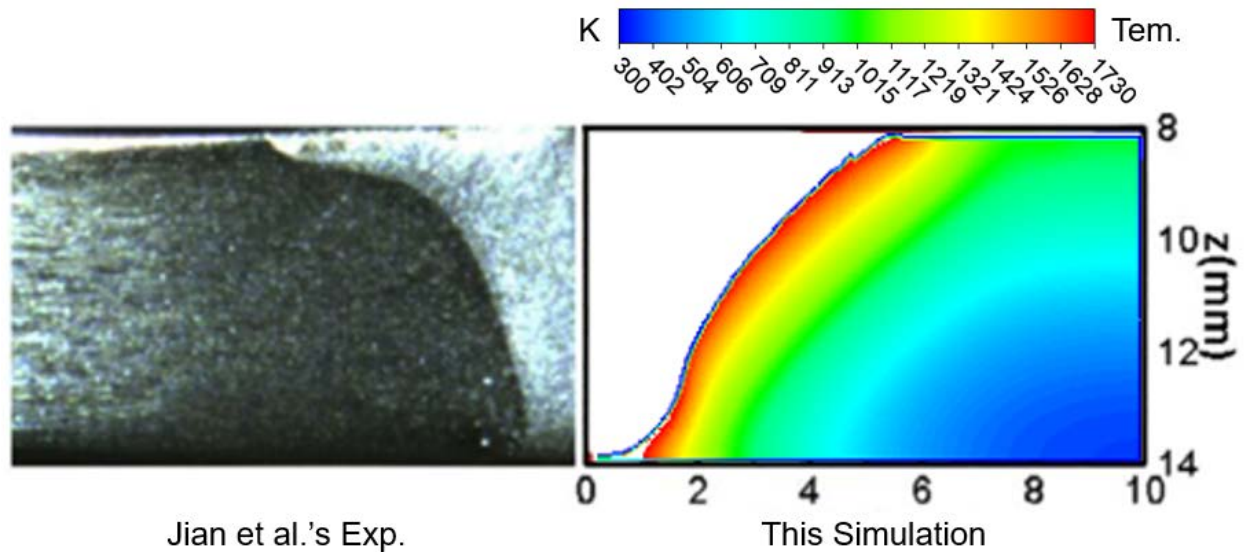
Figure 24. Comparison of the measured and calculated melting profile
at transverse cross-section.

5.7 Results and Discussions

Figure 25 shows the temperature distribution at the axial centerline at different times, which starts from the electrode tip and ends at the bottom of the anode. At the time instant 0.1 s, the arc was not fully developed yet so the temperature reduction after the 0.5 mm is faster than at later times. The plasma arc temperature increases rapidly at the beginning and reaches the maximum value of 28000 K at around 0.5 mm away from the electrode tip. Then, the temperature starts to decrease smoothly and reduce sharply at the anode surface. In this simulation, the arc temperature for 170 A current is much higher than the arc temperature for 200 A current predicted in the simulations conducted in chapter 4. The main reason is that the boundary condition of the current density was treated differently. The simulations in chapter 4 are of a free-burning arc plasma, which did not include the shielding gas; therefore, a profile of current density, which was expressed by Eq. (6), was assigned. However, in this simulation, the shielding gas was considered and the current density was assumed to be uniform at the electrode tip. In the simulations conducted by Pan et al. [7] and Jian et al. [17], the plasma arc simulation with lower current (150 A & 170 A) both produced very similar arc temperature. Since the main purpose of developing this model is to predict the heat transfer between the plasma arc and the anode, in order to validate this model, the boundary

condition used in this simulation was sustained as same as the boundary conditions used in the simulation in the reference paper to the greatest extent.

Figure 26 shows the velocity distribution at the axial centerline at different times, which starts from the electrode tip and ends at the bottom of the anode. The arc column got longer with the penetration of anode by the plasma jet. The highest velocity, which is around 600 m/s, was generated at 2 mm away from the electrode tip after the plasma arc was fully developed. The plasma jet velocity decreased dramatically at the anode pool surface and produced strong stagnation pressure, which is one of the primary reasons that the melted anode was blown away and the keyhole was formed.

Figure 27 shows the radial pressure distribution at the anode surface at different times. The strongest pressure was generated at the central point and it decreased along the radial direction. The most rapid decrease appeared from the very center to the point which is around 2 mm away from the center. At the time instant 0.1 s, since the plasma arc was not fully developed, the unstable arc plasma makes the curve of the radial pressure distribution not very smooth. However, once the plasma arc was fully developed, the whole radial distribution of the pressure follows a Gaussian distribution and the radial pressure distribution was practically the same at different time. Due to the distribution of the arc plasma pressure, the molten pool of the anode at the center was pushed sideways rapidly and the typical cone-like shape of the molten pool was formed.

Figure 28 illustrates the radial total heat flux at the anode surface at different times. The maximum heat flux occurred at the central area and then began reducing towards the sides. However, another local peak was present off the center. Besides the local peak of the total heat flux in the central area, the second peak at the time instant 0.5 s and 1.0 s appeared at 3 mm and 4 mm away from the center, respectively. At the time instant 1.48 s, because the anode was fully penetrated by the arc, the peaks of the total heat flux were observed at around 1 mm and 4 mm away from the center. It is the same for all different times that the total heat flux became very small beyond around 6 mm away from the center. The higher heat flux distribution near the center causes the anode to melt much faster in the central region, which is consistent with the observations of the shape of the molten pool from the experimental work.
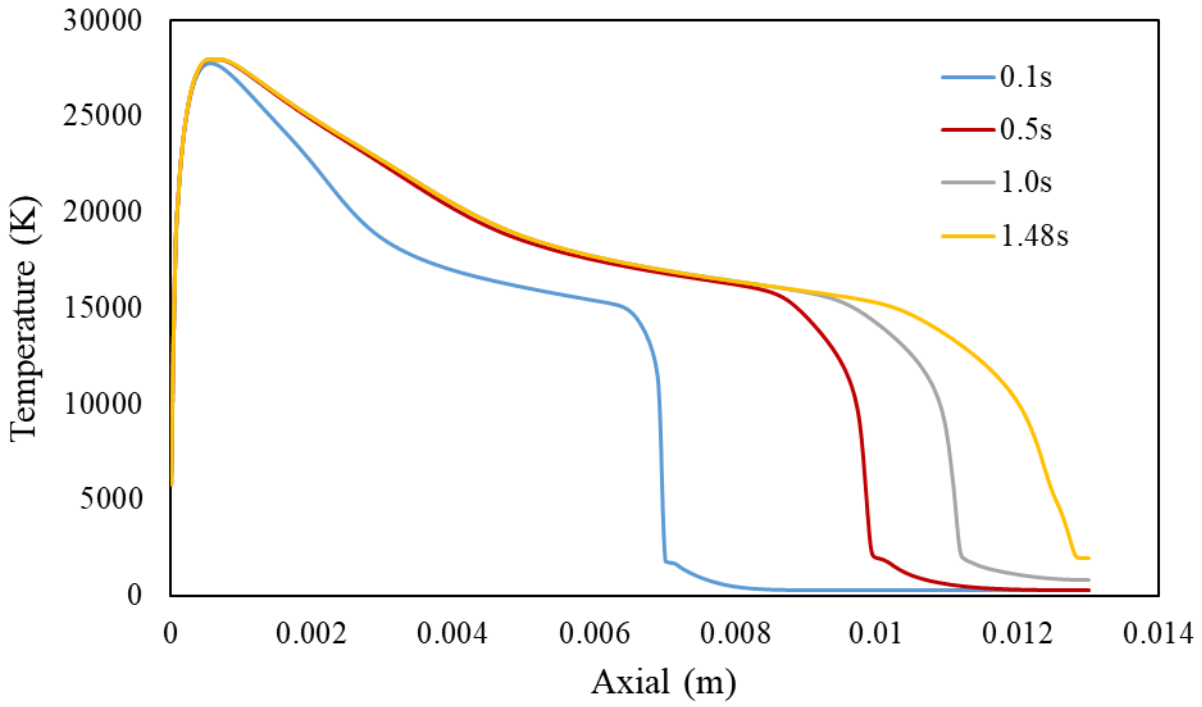
Figure 25. Axial temperature distribution at different times.
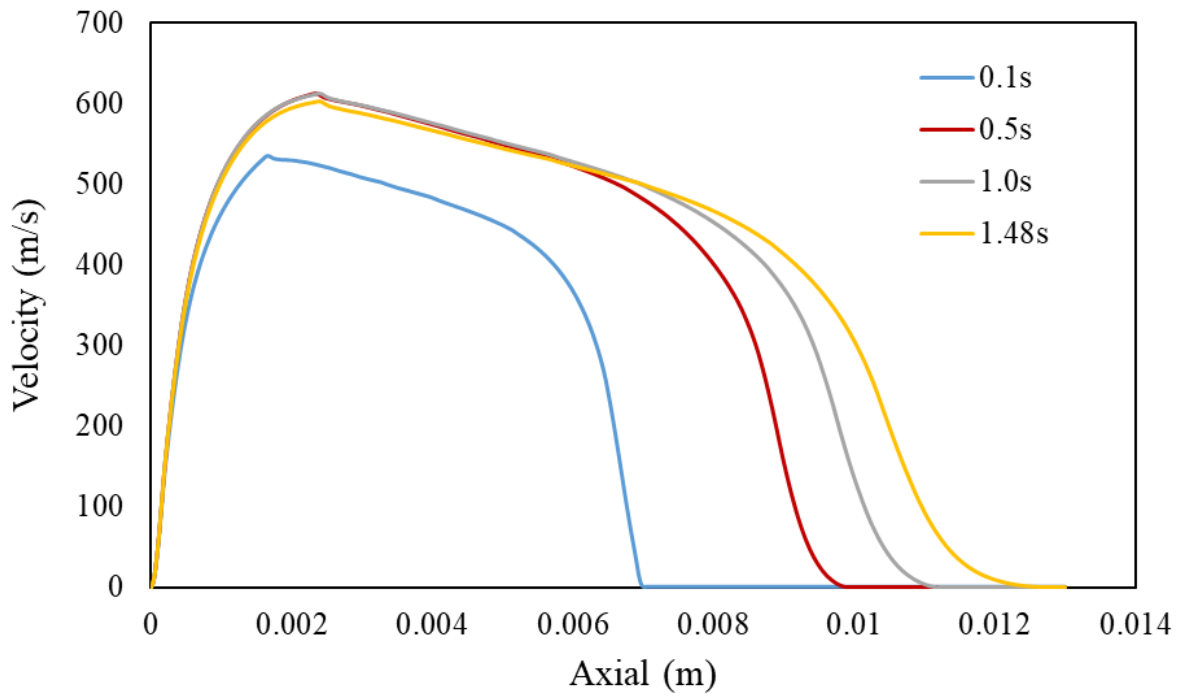
Figure 26. Axial velocity distribution at different times.
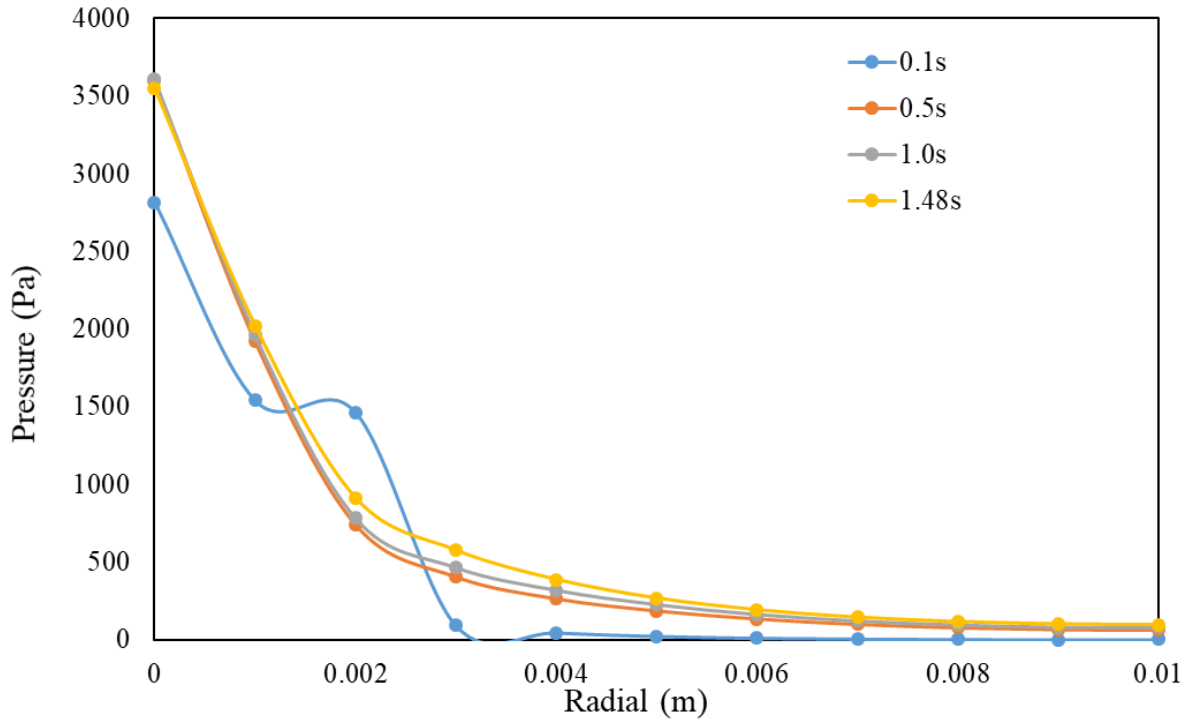
Figure 27. Pressure distribution at the anode surface at different times.
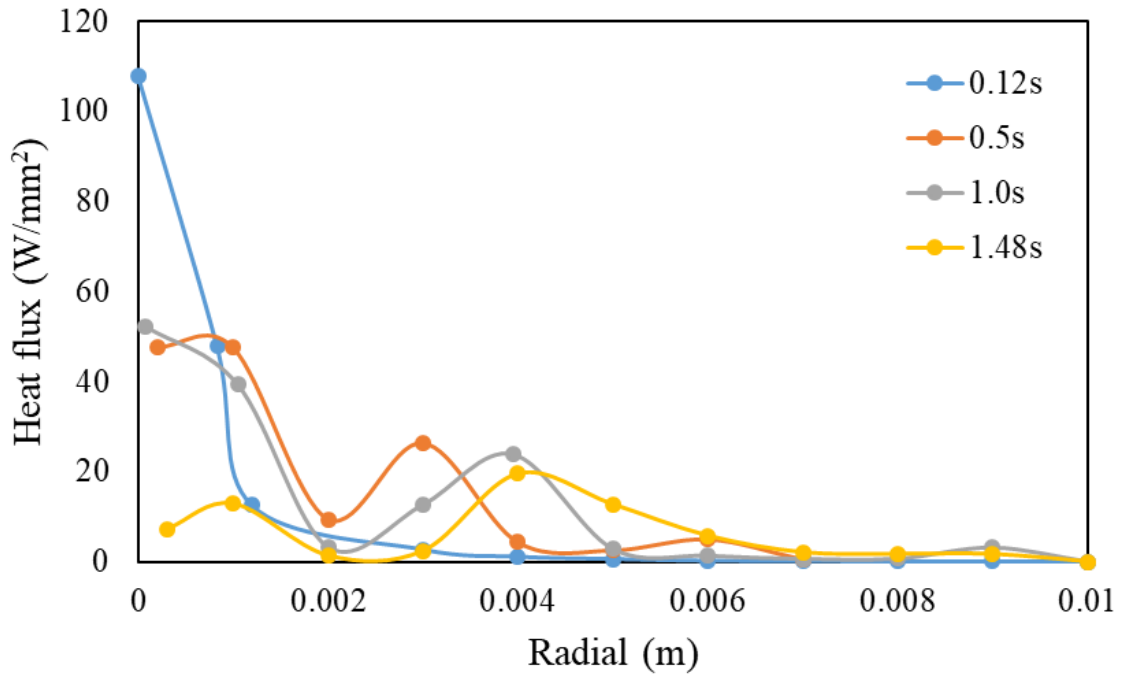

Figure 28. Total heat flux at the anode surface at different times.

5.7.1 Effect of the Current

The metal anode melting behavior is impacted by the arc plasma behavior. However, the characteristic of the arc plasma is closely related with the current used to produce the arc plasma. Therefore, in order to investigate the effect of the arc current on the anode melting behavior, a parametric study of different currents was conducted. In this section, the simulations with current of 140 A and 200 A were developed based on the baseline case in the last section and the results were compared and analyzed.

Figure 29 and Figure 30 illustrate the evolution process of the anode melted by the arc plasma at different times with 200 A current and 140 A current, respectively. As we can see from Figure 29, the anode was penetrated by the plasma arc at about 1.21 s when the 200 A current was used. With impact of the plasma arc, the diameter of the keyhole at the anode bottom kept increasing. For the arc with 140 A current in Figure 30, the anode was penetrated by the arc plasma at 1.92 s and the penetration rate was slower than others. The penetration also reflects the melting rate of the anode. Comparing the penetration time among the simulation with current 140 A, 170 A and 200 A in Figure 33, it can be said that with the current increase, the penetration time of the anode decreases almost linearly.

Figure 31 shows the axial centerline temperature distribution from the electrode tip to the anode bottom with different current at 0.1 s. With different current, the same tendency of the variation of the axial centerline temperature was observed. However, it is very obvious that with the larger current, the arc temperature becomes higher as well. The higher temperature of the arc will increase the temperature difference between the arc plasma and the anode, which will also enhance heat transfer between the arc plasma and the anode. In Figure 34, the highest temperature with different current was compared and it is found that there is a positive correlation between the arc temperature and the current.

Figure 32 shows the axial centerline velocity distribution from the electrode tip to the anode bottom with different current at 0.1 s. With the current varying, the variation trends of the axial centerline velocity are consistent, but with the stronger current, the velocity of the plasma jet is higher, which means the plasma jet will bring more intense momentum and the impingement of the plasma jet

on the anode will be more drastic. In addition, the splashing of the molten pool in the anode will be fiercer and the convection heat transfer between the arc plasma and the anode will be enhanced as well. From Figure 35, it is observed that with the current increase, the highest arc velocity increases linearly. Based on the effect of the current on the arc velocity and the arc temperature, it can be said that it is reasonable that with higher current, the anode will be penetrated more quickly, which also imply that the melting rate of the metal anode increases with the current of the plasma arc increase.
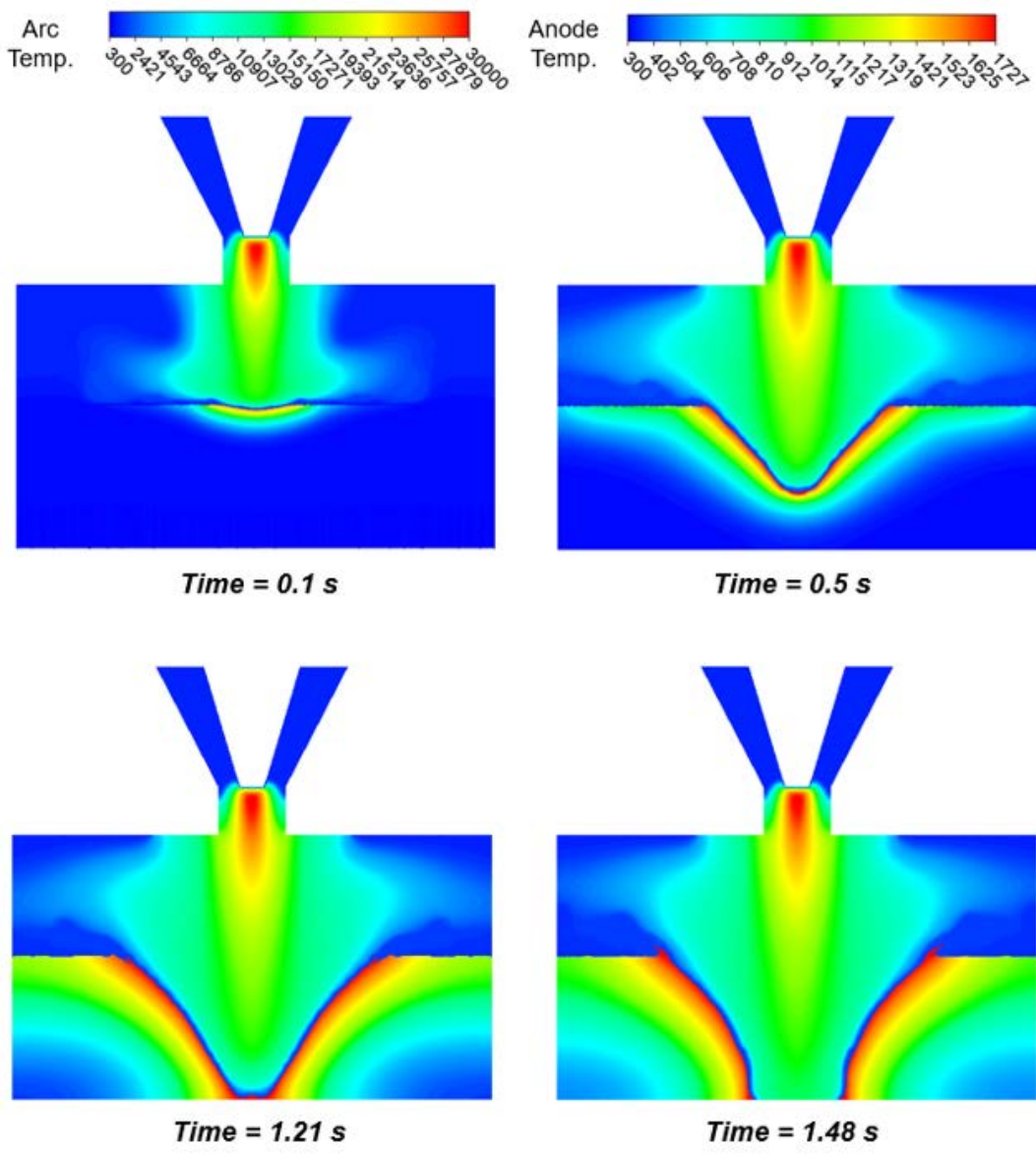

Figure 29. Melting process of the metal anode utilizing the arc plasma at different times with 200 A current.
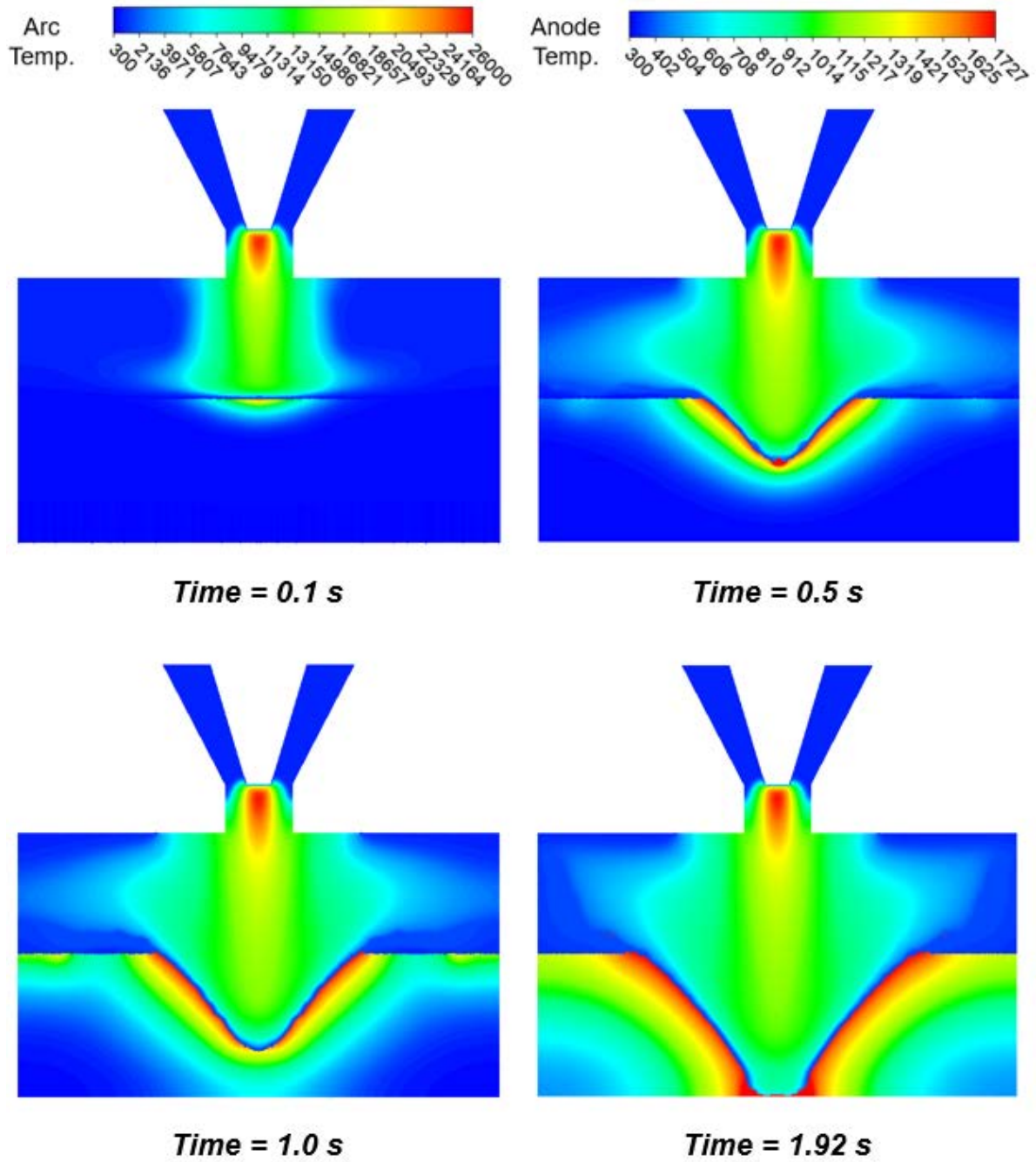
Figure 30. Melting process of the metal anode utilizing the arc plasma at different times with 140 A current.
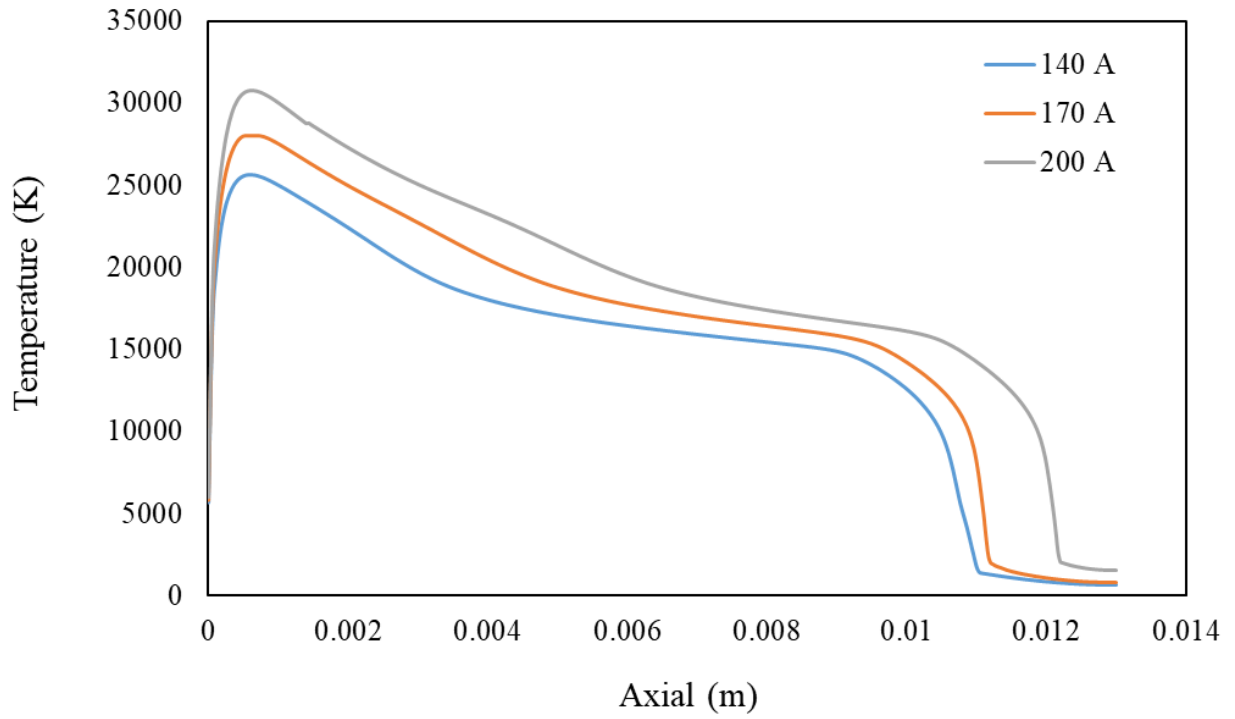
Figure 31. Axial temperature distribution with different current at 0.1 s.
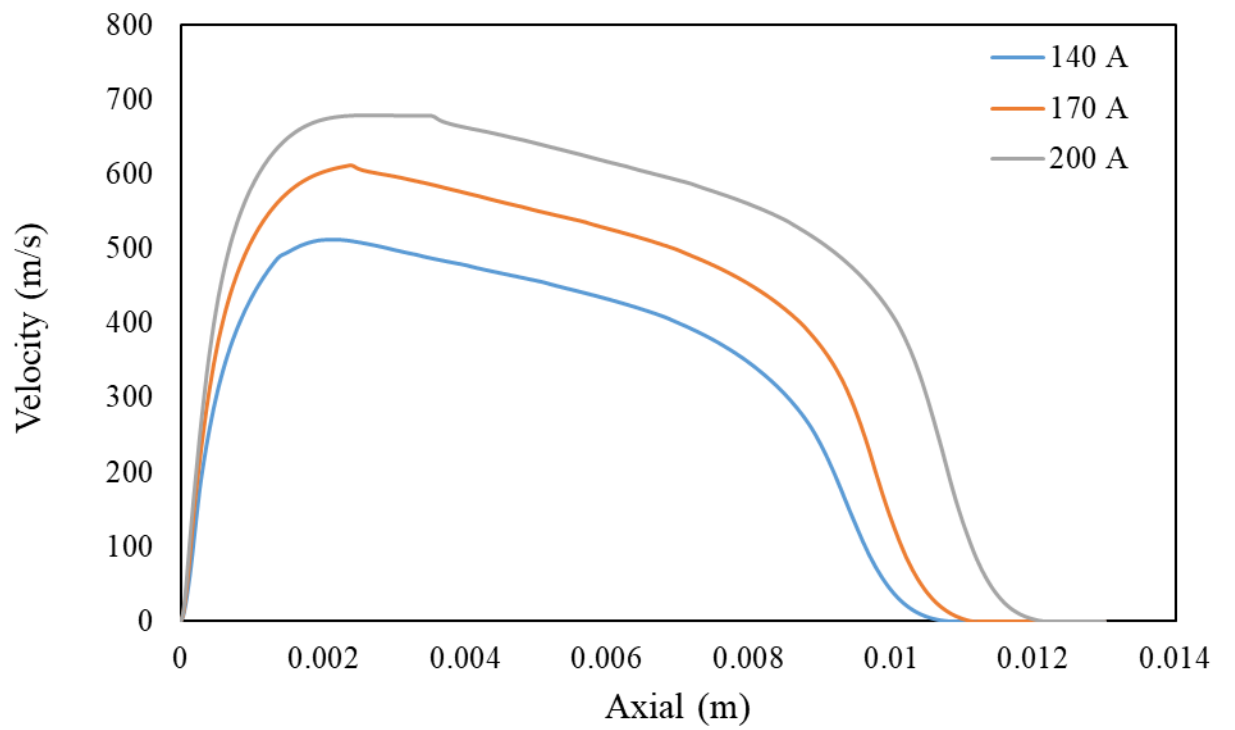
Figure 32. Axial velocity distribution with different current at 0.1 s.
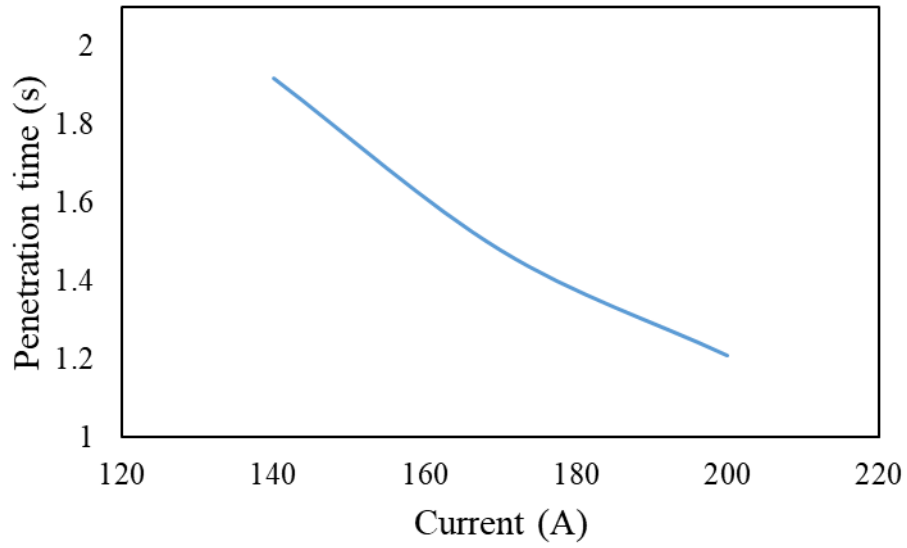
Figure 33. The effect of the current on the penetration time.
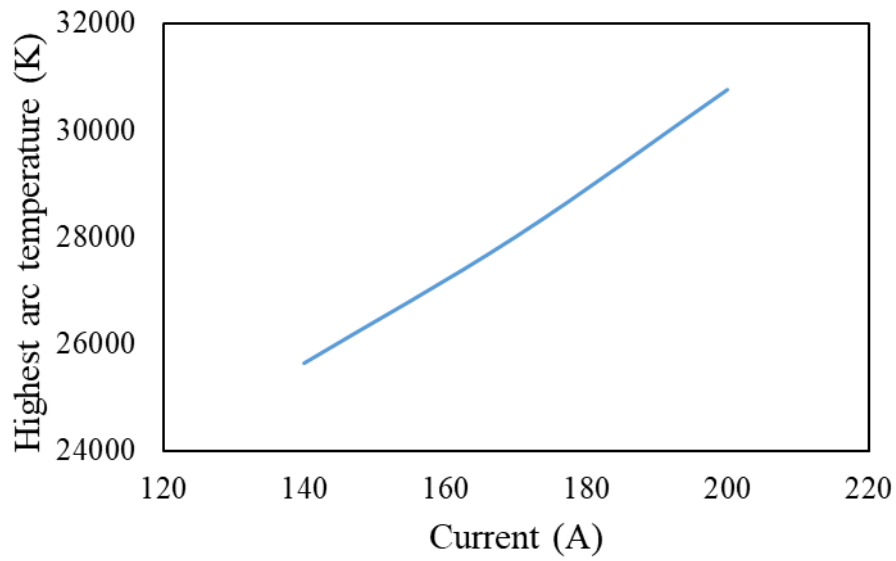

Figure 34. The effect of the current on the highest arc temperature.
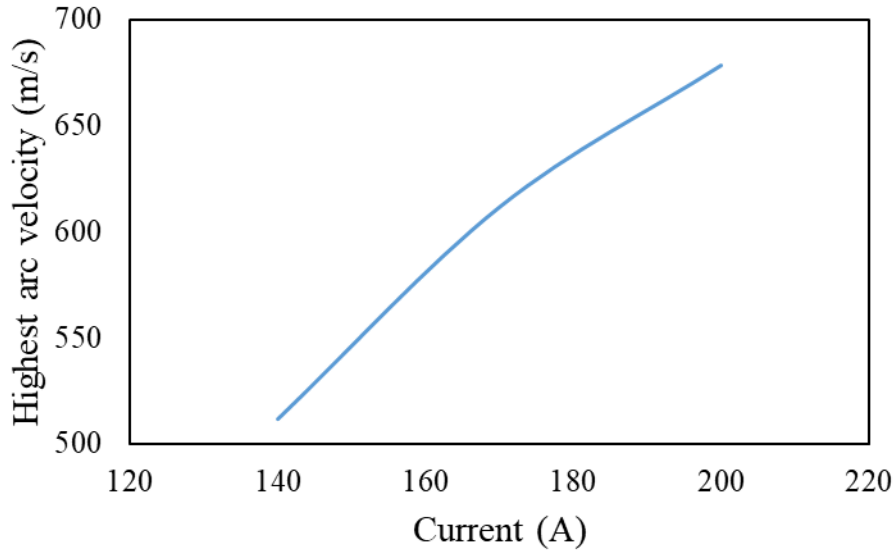
Figure 35. The effect of the current on the highest arc velocity.

5.7.2 Effect of the Metal Anode Initial Temperature

In the industrial steelmaking process such as the EAF steelmaking process, the melting time of the scrap is very important which determines the productivity. The reduction of the scrap melting time will increase the productivity of the steel making in the EAF process. Therefore, in order to investigate the factors affecting the melting rate of the anode, the different anode initial temperatures were studied. The simulations with different initial temperatures of the anode for 300 K, 600 K and 900 K were conducted under 170 A arc current and the results were discussed and compared.

Figure 36 (a) presents the evolution process with 600 K initial anode temperature. As the temperature contours are showing, the anode was penetrated by the arc plasma at 1.37 s. Compared to baseline case in which the anode initial temperature is 300 K, the penetration time was slightly shortened. In Figure 36 (b) that shows the evolution process with 900 K initial anode temperature, the anode was penetrated by the arc plasma at 1.24 s, which was faster than the other two. Figure 37 shows the axial centerline temperature distribution from the electrode tip to the anode bottom with different initial anode temperature at 0.1 s. In this figure, it is clear that the higher initial anode temperature will lead to faster penetration of the anode. At 0.1 s, the plasma arc can reach around

63

12 mm away from the electrode tip. In Figure 38, relationship between the penetration time of the anode and different initial anode temperature was illustrated. With higher initial anode temperature, the penetration time will be shorter.
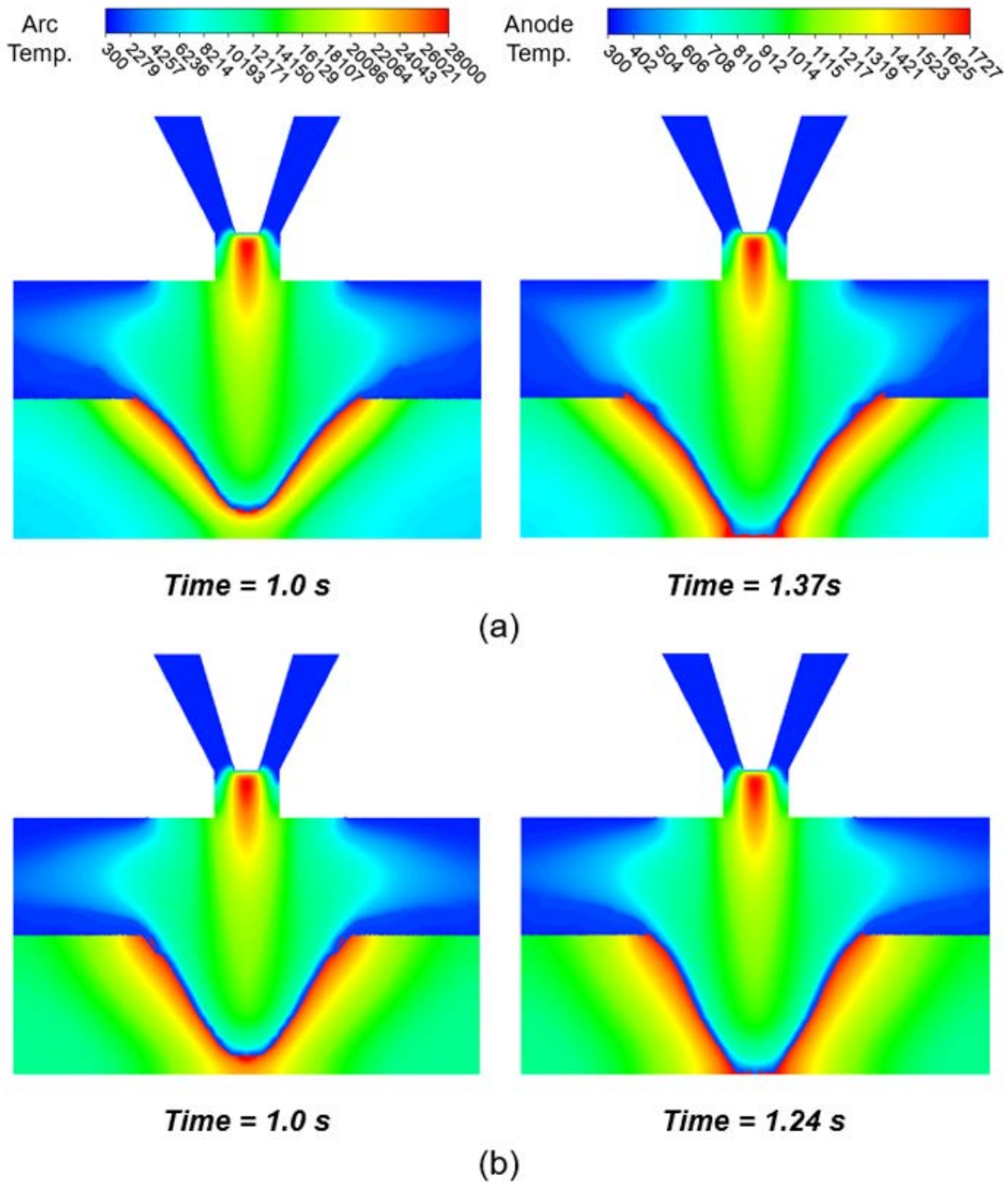

Figure 36. Melting process of the anode utilizing the arc plasma at different times
with 170 A current (a) initial anode temperature 600 K (b) initial anode temperature 900 K.
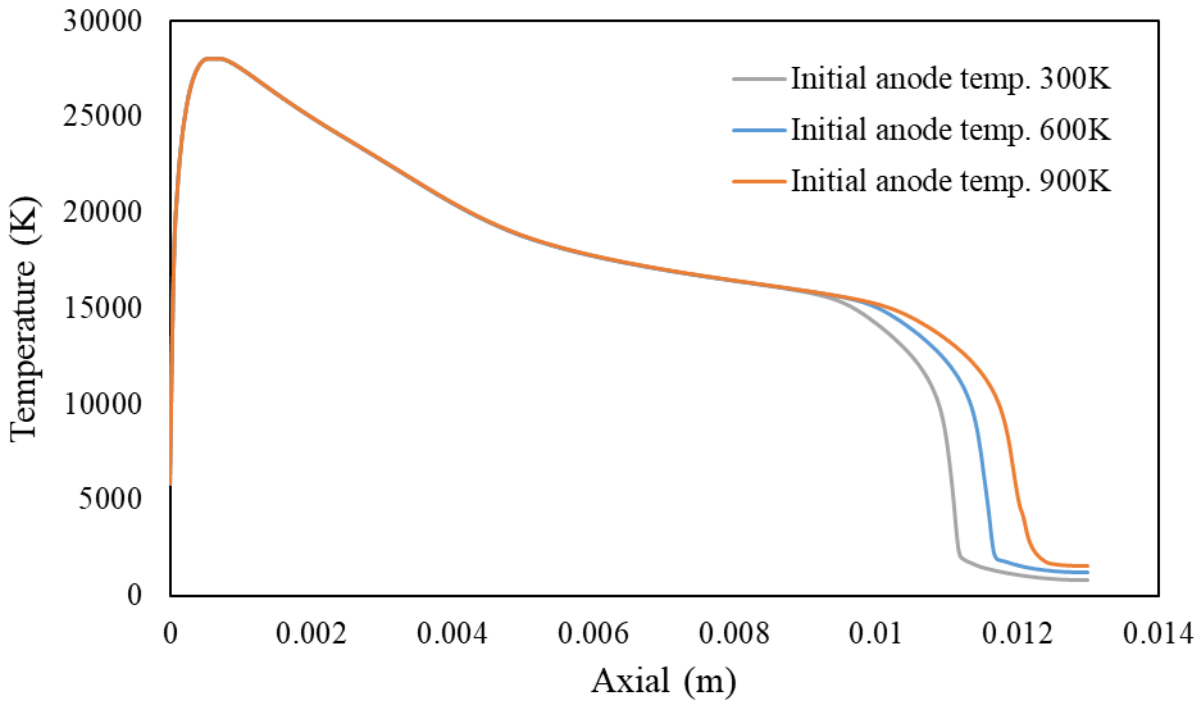
Figure 37. Axial temperature distribution with different initial anode temperature at 0.1 s.
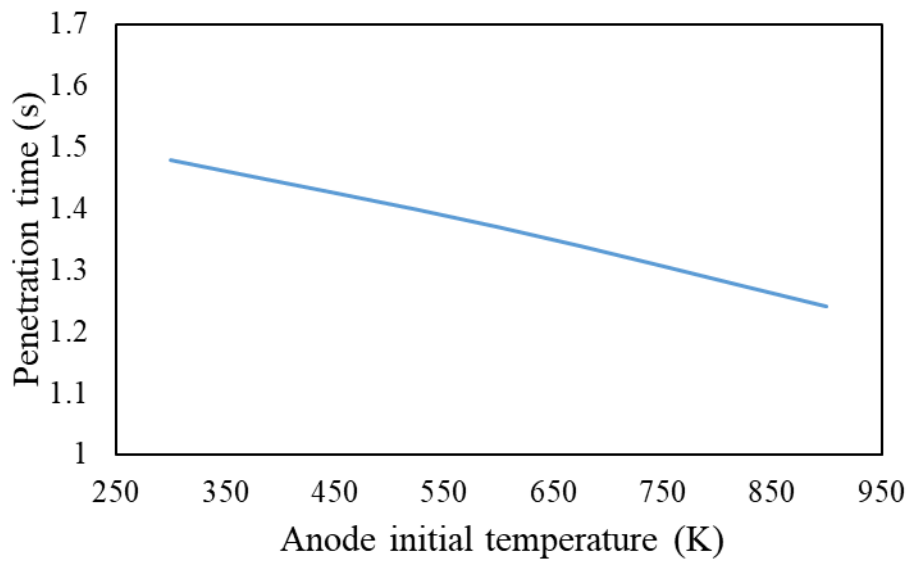

Figure 38. The effect of the initial anode temperature on the penetration time.

CHAPTER 6. CONCLUSIONS

The present study numerically analyzed the behavior of the DC electric plasma arc and the evolution process of the metal anode melted by the plasma arc. The MHD provides the theoretical support with the development of the free-burning arc model. The interface tracking by the VOF method provides the possibility with the implementation of the heat transfer from the plasma arc to the metal anode. The enthalpy-porosity technique was used to capture the melting phenomenon. Furthermore, the parametric studies for the heat transfer between the plasma arc and the anode have been performed. Finally, the work in the present study can be concluded:

1. A two-dimensional and three-dimensional DC electric arc model has been developed and validated by comparing with the experimental data.

2. The arc-metal heat transfer model has been developed and the corresponding validation has been conducted by comparing with experimental observation.

3. The phenomenon of the metal melting process by electric arc plasma has been captured and analyzed.

4. The effect of the arc current was investigated and it was found that with the increase in the arc current, the temperature and velocity of the plasma arc increase and the metal anode penetration time decreases.

5. The effect of the initial metal temperature was investigated and it was found that for higher initial anode temperature, the penetration time of the metal anode will be shortened.

REFERENCES

1. Florian and T. Peter: "Physics-Based Modeling of Electric Operation, Heat Transfer, and Scrap Melting in an AC Electric Arc Furnace", *Metallurgical and Materials Transactions B*, Vol. 47, pp. 1489–1503, 2016.

2. J. Oda, K. Akimoto and T. Tomoda: "Long-term Global Availability of Steel Scrap", Resour. Conserv. Recycl., Vol. 81, pp. 81–91, 2013.

3. E. Pretorius et al.: "EAF Fundamentals"

4. Z. Guo, W, Zhao: "Arc and thermal plasma", *Beijing: Science Publish*, 1986

5. J. Mckelliget and J. Szekely, "Heat transfer and fluid flow in the welding arc", *Metallurgical Transactions*, vol. 17A, pp.1986-1139, 1986.

6. T. Zacharia, S.A. David, J.M. Vitek, "Effect of evaporation and temperature dependent material properties on weld pool development", *Metall. Transf.* Vol. B 22, pp. 233–241, 1992.

7. J. Pan, S. Hu, L. Yang and S. Chen, "Numerical analysis of the heat transfer and material flow during keyhole plasma arc welding using a fully coupled tungsten-plasma-anode model", *Acta Materialia*, Vol. 118, pp.221-229, 2016.

8. K. C. Hsu, K. Etemadi and E. Pfender, "Study of the free-burning high-intensity argon arc", *American Institute of Physics*, 53(3), 1983.

9. L. Sansonnens, J. Haidar and J. J. Lowke, "Prediction of properties of free burning argon arcs including effects of ambipolar diffusion", J. Phys. D: Appl. Phys. Vol. 33, pp. 148, 2000.

10. J. J. Lowke and M Tanaka, "LTE-diffusion approximation for arc calculations", *Institute of Physics*, Vol. 39, pp. 3634-3643, 2006.

11. F Lago, J. J. Gonzalez, P. Freton and A. Gleizes, "A numerical modelling of an electric arc and its interaction with the anode: Part I. The two-dimensional model", *Institute of Physics*, Vol. 37, pp. 883-897, 2004.

12. J. J. Gonzalez, F Lago, P. Freton, M. Masquere and X. Franceries, "Numerical modelling of an electric arc and its interaction with the anode: part II. The three-dimensional model—influence of external forces on the arc column", *Institute of Physics*, Vol. 38, pp. 306-318, 2005.

13. L. Li, B. Li, L. Liu and Y. Motoyama, "Numerical Modeling of Fluid Flow, Heat Transfer and Arc–Melt Interaction in Tungsten Inert Gas Welding", *High Temperature Materials and Processes*, 2017.

14. R. T. C. Choo, J. Szekely and R. C. Westhoff, "Modeling of high-current arcs with emphasis on free surface phenomena in the weld pool", *Welding Research Supplement*, 1990.

15. P Freton, J J Gonzalez and A Gleizes, "Comparison between a two- and a three-dimensional arc plasma configuration", *J. Phys. D: Appl. Phys.*, Vol. 33, pp. 2442-2452, 2000.

16. Y. Li, L. Wang and C. Wu, "A novel unified model of keyhole plasma arc welding", *International Journal of Heat and Mass Transfer*, Vol. 133, pp. 885-894, 2019.

17. X. Jian and C. Wu, "Numerical analysis of the coupled arc–weld pool–keyhole behaviors in stationary plasma arc welding", *International Journal of Heat and Mass Transfer*, Vol. 84, pp. 839-847, 2015.

18. M. Tanaka, H. Terasaki, M. Ushio and J. J. Lowke, "Numerical Study of a Free-burning Argon Arc with Anode Melting", *Plasma Chemistry and Plasma Processing*, Vol. 23, No. 3, 2003.

19. H. J. Odenthal, A. Kemminger, F. Krause, L. Sankowski, N. Uebber, and N. Vogl, "Review on Modeling and Simulation of the Electric Arc Furnace (EAF)," *Steel Res. Int.*, vol. 89, no. 1, p. 1700098, 2018.

20. J. Oda, K. Akimoto, and T. Tomoda, "Long-term Global Availability of Steel Scrap," *Resour. Conserv. Recycl.*, vol. 81, pp. 81–91, 2013.

21. J. Alexis, M. Ramirez, G. Trapaga and P. Jonsson, "Modeling of a DC Electric Arc Furnace-Heat Transfer from the Arc", *ISIJ International*, Vol. 40, pp. 1089-1097, 2000.

22. F. Wang, Z. Jin and Z. Zhu, "Numerical Study of DC Arc Plasma and Molten bath in DC Electric Arc Furnace", *Ironmaking and Steelmaking*, Vol 33, No. 1, 2006.

23. M. Goodarzi, R. Choo, T. Takasu, J.M. Toguri, "The Effect of the Cathode Tip Angle on the Gas Tungsten Arc Welding Arc and Weld Pool: II. The Mathematical Model for the Weld Pool", *J. Phys. D. Appl. Phys*. Vol. 31, pp. 569–583, 1998.

24. X. Wang, D. Fan, J. Huang, Y. Huang, "A Unified Model of Coupled Arc Plasma and Weld Pool for Double Electrodes TIG Welding", *J. Phys. D. Appl. Phys*. Vol.47, pp. 14, 2014.

25. M. Tanaka, K. Yamamoto, S. Tashiro, et al., "Time-dependent calculations of molten pool formation and thermal plasma with metal vapour in gas tungsten arc welding", *J. Phys. D: Appl. Phys.* Vol. 43, pp. 434009–434020, 2010.

26. J. Hu and H.L. Tsai, "Heat and Mass Transfer in Gas Metal Arc Welding. Part I: The Arc", *International Journal of Heat and Mass Transfer*, Vol. 50, pp. 833-846, 2007.

27. X. Jian, C. Wu, G. Zhang and J. Chen, "A Unified 3D Model for an Interaction Mechanism of the Plasma Arc, Weld Pool and Keyhole in Plasma Arc Welding", *Journal of Physics D: Applied Physics*, Vol. 48, pp. 14, 2015.

28. M. I. Boulos, P. Fauchais and E. Pfender, "Thermal Plasmas Fundamentals and Applications", Vol. 1, 1994.

29. M. A. Ramirez, G. Trapaga and J. McKelliget, "A comparison between two different numerical formulations of welding arc simulation Model", *Simul. Mater. Sci. Eng*., Vol. 11, pp. 675–95, 2003.

30. H. G. Fan and R Kovacevic, "Keyhole formation and collapse in plasma arc welding", *Journal of Physics D: Applied Physics*, Vol. 32, pp. 2902-2909, 1999.

31. J. J. Lowke, R. Morrow and J. Haidar, "A simplified unified theory of arcs and their electrodes", *Journal of Physics D: Applied Physics*, Vol. 30, pp. 2033-2042, 1997.

32. M. Tanaka, H. Terasaki, M. Ushio, and J. J. Lowke, "A unified numerical modeling of stationary tungsten-inert-gas welding process", *Metallurgical and Materials Transactions A*, Vol. 33A, pp. 2002-2043, 2001.

33. X. Wang, Y. Luo and D. Fan, "Investigation of heat transfer and fluid flow in high current GTA welding by a unified model", *International Journal of Thermal Sciences*, Vol. 142, pp. 20-29, 2019.

34. M. Ushio and C.S. Wu, "Mathematical modeling of three-dimensional heat and fluid flow in a moving gas metal arc weld pool", *Metallurgical and Materials Transactions B*, Vol. 28B, pp. 1997-509, 1995.

35. T. Zhang, C. S. Wu and Y. Feng, "Numerical Analysis of Heat Transfer and Fluid Flow in Keyhole Plasma Arc Welding", *Numerical Heat Transfer, Part A*, Vol. 60, pp. 685-698, 2011.

36. D. L. Youngs, "Time-dependent Multi-material Flow with Large Fluid Distortion", *Numerical Methods for Fluid Dynamics*, pp. 273-285, 1982.

37. D. Wu, S. Tashiro, X. Hua and M. Tanaka, "Analysis of the energy propagation in the keyhole plasma arc welding using a novel fully coupled plasma arc-keyhole-weld pool model", *International Journal of Heat and Mass Transfer*, Vol. 141, pp. 604-614, 2019.

38. L. Gu, Y. Zhu, G. He, A. Farhadi and W. Zhao, "Coupled numerical simulation of arc plasma channel evolution and discharge crater formation in arc discharge machining", *International Journal of Heat and Mass Transfer*, Vol. 135, pp. 674-684, 2019.

39. S. Tashiro, M. Miyata and M. Tanaka, "Numerical analysis of AC tungsten inert gas welding of aluminum plate in consideration of oxide layer cleaning", *Thin Solid Films*, Vol. 519, pp. 7025-7029, 2011.

40. H. X. Wang, Y. H. Wei and C. L. Yang, "Numerical calculation of variable polarity keyhole plasmaarc welding process for aluminum alloys based onfinite difference method", *Computational Materials Science*, Vol 40, pp. 213-225, 2007.

41. X. Wang, J. Huang, Y. Huang, D. Fan and Y. Guo, "Investigation of heat transfer and fluid flow in activating TIG welding by numerical modeling", *Applied Thermal Engineering*, Vol. 113, pp. 27-35, 2017.

42. Z. M. Liu, S. Cui, Z. Luo, C. Zhang, Z. Wang and Y. Zhang, "Plasma arc welding Process variants and its recent developments of sensing controlling and modeling", *Journal of Manufacturing Processes*, Vol. 23, pp. 315-327, 2016.

43. Y. Li, Y. Feng, X. Zhang and C. Wu, "An evolutionary keyhole-mode heat transfer model in continuous plasma arc welding", *International Journal of Heat and Mass Transfer*, Vol. 117, pp. 1188-1198, 2018.

44. Y. Li, Y. Feng, X. Zhang and C. Wu, "An improved simulation of heat transfer and fluid flow in plasma arc welding with modified heat source model", *International Journal of Thermal Sciences*, Vol. 64, pp. 93-104, 2013.

45. A. Farzadi, S. Serajzadeh and A. H. Kokabi, "Modeling of heat transfer and fluid flow during gas tungsten arc welding of commercial pure aluminum", *International Journal of Advanced Manufacturing Technology*, Vol. 38, pp. 258-267, 2008.